Enhancing In-Flight Structural Health Monitoring of Vertical Lift Vehicles Operating in an Urban Environment

Godfrey Sauti
Research Materials Engineer
NASA Langley Research Center
Hampton, VA, U.S.A.

Russell A. Wincheski
Research Materials Engineer
NASA Langley Research Center
Hampton, VA, U.S.A.

Christopher J. Stelter
Research Materials Engineer
NASA Langley Research Center
Hampton, VA, U.S.A.

Michael R. Horne
Materials Engineer, Senior
Analytical Mechanics Associates
Hampton, VA, U.S.A.

Jason P. Moore
Research Materials Engineer
NASA Langley Research Center
Hampton, VA, U.S.A.

Emilie J. Siochi
Research Materials Engineer
NASA Langley Research Center
Hampton, VA, U.S.A.

ABSTRACT

In-situ airframe sensors have long been considered a potential solution for structural health monitoring that could change the design, certification, operation and maintenance paradigms of flight vehicles. In this approach, large networks of sensors covering the entire, or most of, an airframe throughout its operational lifetime would support real-time decisions on airworthiness and obviate the need to overbuild components or perform multiple cycles of structural qualification testing and inspections. This concept would go beyond the current practice of placing select sensors in strategic locations or relying on such sensors only during airframe qualification flights and inspections. For vehicles in the emerging urban air mobility space, reducing weight associated with overbuilds and shortening down-time associated with inspections are critical for improving safety and affordability. In practice, the wide-scale use of in-situ sensors as primary assurance for structural health has not been demonstrated to be feasible or the best solution. A sensor integration testbed was developed as a platform to evaluate the potential of multiple sensor types to enable decision making on airworthiness. We report on the initial runs of this testbed with multiple sensors attached to a common test article. Metal foil strain gauges, eddy current, fiber optic, guided wave (acoustic emission and ultrasonic) and carbon nanotube roving sensors were affixed to the test article. Baseline as well as post damage initiation and fatiguing data are presented and discussed. Despite the relative simplicity of the test article, the interpretation of the as-captured test data was generally not conclusive or did not have wide enough coverage. This result emphasizes the challenges and current limitations both in testing and the practical broad application of embedded sensors as the determinative elements in critical decision making on wide-scale structural health.

INTRODUCTION

The fast-developing urban air mobility (UAM) market will drive operators and innovators to develop varied airframes as they seek to improve performance margins and gain a competitive edge. These airframes, which include complex configurations, will likely not benefit completely from the legacy data sets that have been established for the performance of commercial transport scale, traditional tube and wing, as well as rotary wing designs (Refs. 1–3). Although there have been studies on factors that will influence the implementation of UAM, most are focused on barriers such as regulatory policy, user acceptance, ground infrastructure and air traffic management (Refs. 4, 5). There is much less attention given to structural health maintenance, which forms the basis for aircraft airworthiness determination in large transport aircraft (Ref. 6). Furthermore, in the UAM scenario, small aircraft may be flying at lower altitudes where the damage characteristics are different from those currently encountered in large commercial transport or larger rotary aircraft. In addition to the differences in heritage and UAM flight regimes, the search for improved performance in UAM, which includes a fast turnaround on the introduction of new designs, will likely lead to the deployment of airframes that do not have millions of flight hours of testing. In this emerging flight architecture, structural state awareness and eventual autonomy enabled by sensors and in-flight decision making can potentially mitigate risk.

Sensor-Enabled Health Monitoring

In this paper, the investigation of an operational paradigm that enables safe flight through the integration of damage detection sensors into the airframe to provide real-time information on its structural state throughout its lifetime is presented. It has been hypothesized that sensor data can be analyzed to adjust maintenance intervals and predict remaining service life. Current aviation practice to assure structural integrity is largely

Presented at the Vertical Flight Society's 6th Decennial Aeromechanics Specialists' Conference, Santa Clara, CA, Feb. 6-8, 2024.

dependent on ground inspections during regularly scheduled maintenance (Ref. 7), with structural sensors in limited use at critical locations on specific aircraft (Ref. 8). While aircraft may be heavily instrumented during qualification testing, much of the airframe sensor suite is removed prior to fleet delivery.

In the aircraft envisioned for the UAM market, it is likely that a more agile system will be required. Flight safety decisions based on real-time structural performance data specific to the actual flight history of each individual aircraft could provide more accurate information of the state of the structure. This capability will be especially important in an operational environment where there will be much greater diversity of flight history than currently seen in the commercial transport market.

A proposed approach involves the integration of a sensor suite to monitor structural health of the aircraft during flight to detect and report structural damage. The report could be delivered to the crew, maintenance personnel and/or to a flight management system that is capable of processing information of the structural state relative to the design envelope of the vehicle. It must be emphasized that there is a *hierarchy* of potential responses/respondents to in-flight events such as those that could be detected by the sensors, as shown schematically in Figure 1. This hierarchy determines requirements such as the response speed and the size/weight of supporting instrumentation for the sensors or other subsystems related to those events and where/when their data gets processed. As an example, systems that provide data for the maintenance database may not be required to respond as fast as those providing data for in-flight decision making. In addition, such systems may not be required to reside on-board in a flight configuration, widening the available component space while reducing costs. On the other-hand, for sensor systems that are expected to be used in flight, it is critical that the weight, volume, and power requirements are practical for on-board use and all components can meet flight qualification standards. The final processed data product throughput must support the time-scales for in-flight decisions. Appreciating the different requirements for the steps in this hierarchy is critical to arriving at practical technology options for the associated systems.

While in-flight reaction to structural (propulsor) damage has been demonstrated in quadcopter wind tunnel experiments (Ref. 9), a wider scoping and more actionable structural health monitoring (SHM) implementation has remained a challenge in spite of significant research in the area (Refs. 10–12).

The use of large networks of in-situ sensors has always been an attractive option for SHM in "self-aware" structures and vehicles (Refs. 13–16), but many important questions remain:

- What sensor types are needed? What are their physical measurands?
- How do the sensor measurands translate to the structural state?

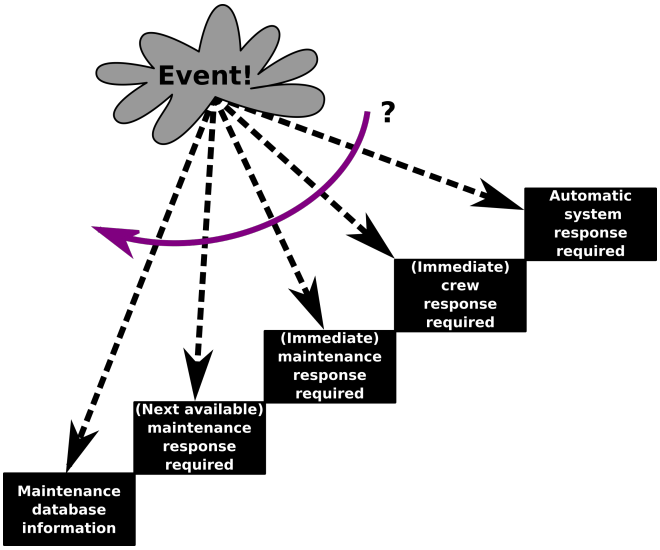

Figure 1. The diagram shows a hierarchy of potential responses/respondents to in-flight events detected by in-situ structural health sensors.

- How many sensors?
- Where should the sensors be located?
- What should the physical response rate of the sensors be?
- What is the required reading rate for the data acquisition systems associated with the sensors?
- At what rate should raw sensor data be initially processed?
- What speed is required for higher level data processing to translate sensor data into structural information?
- What is the substance of the final data product?
- How will the final sensor data product be tied to the state of the structure and any action?
- If thresholds are used, how should they be set?
- Under which operational conditions will the sensors provide reliable data?
- Under what conditions will the sensors not provide reliable data and what should be done then?
- How should false positives/false negatives be handled?
- What are the effects of sensor lifetime and any sensor failures?
- What should be done about sensor maintenance and redundancy?
- What is the size, cost, weight of the sensors and associated equipment including wiring harnesses and additional processing capability?

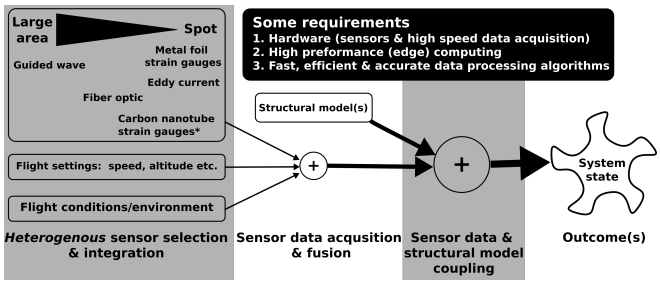

Figure 2. The fusion of data from different sensor types is required to make decisions on the state of a structure with high confidence.

Obtaining answers to these questions, which is critical in the potential wider use of sensors for SHM, has proved elusive. In aerospace, these questions lie at the intersection of different domains, some of which are *Structures*, *Materials*, *Sensors/Nondestructive Evaluation* and *Controls*. Each of the domains has different capabilities and limitations which are not always very well communicated across the disciplines. The small sensor, fast and accurate data processing, as well as failure prediction and mitigation capabilities, required for the envisaged SHM application are also at the extreme limit of what is currently possible in each domain. Therefore, the formulation of real requirements has been something of a chicken and egg problem. Examples of this are questions of how fast the data need to be provided versus the smallest size of feature detectable and the area covered. *"Capture and provide data on the smallest damage event as soon as it occurs anywhere over the entire airframe and at any point during flight operations"* is not a practical set of actionable requirements.

In-flight vehicle structural health-based decision making to assure safe operations of UAM vehicles will, if feasible, most likely require the fusion of data from multiple sensor types as shown schematically in Figure 2. The use of multiple sensor types can potentially provide detection of impact, fatigue, and overstrain events at both critical locations and globally over the aircraft structure. No single sensor type has been demonstrated to be able to provide unambiguous information on a structure's health under all envisaged operational conditions with enough confidence and coverage for decisions on that health. To make decisions with a higher degree of confidence, the data from multiple sensors must be intelligently fused to obtain a more complete picture of the vehicle state. Even given the potential use of multiple sensor types, it is not guaranteed that they will be adequate to provide the requisite information with enough confidence for decision making throughout the entire operational envelope and lifetime of the airframe. Sensor data fusion in turn is a complex challenge, especially under the operational and computational resource limitations of a UAM vehicle.

Testing new technologies/paradigms

There are several stages/pathways to assessing the feasibility of using new technologies in aviation as shown in Figure 3. In

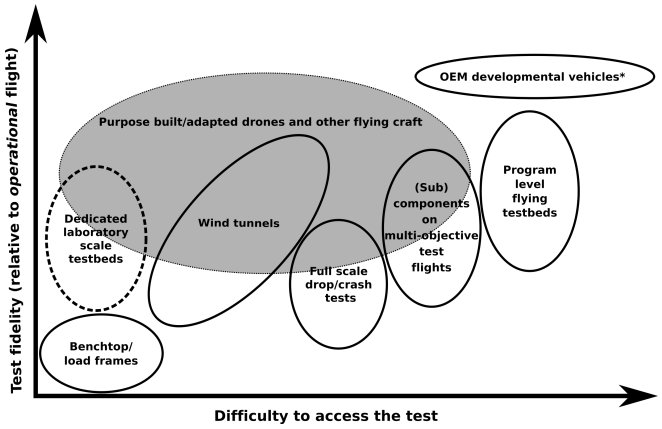

Figure 3. In general, the evaluation fidelity of new sensor technology is directly dependent on the complexity of testing, and testing costs are often exponentially dependent on test complexity.

the figure, the fidelity of the testing, i.e., its ability to address a particular set of questions, is mapped against the degree of difficulty in accessing the test. The mapping is on an arbitrary scale with a focus on the requirements for testing sensor enabled SHM.

Difficulty to access the test includes:

1. Test approval requirements
2. Frequency at which the tests are conducted, e.g., piggybacking on other programs/tests may be necessary
3. If piggybacking on other tests, how well the sensor testing, which is often not the primary test, integrates with the other tests
4. If piggybacking, the availability of real-estate on the test platform for (multiple) sensor installation, data capture equipment and data channels
5. The ability to iterate/change out test components
6. The ability to set desired load/damage profiles
7. The ability to model the expected structural response in support of the testing (the more complex the test article the harder this is)
8. Level of preparation required before accessing the facility - dealing with unknowns of the exact test setup
9. Scheduling - when the experiments might be able to get done can be critical to program level decision making

Test fidelity includes:

1. The physical test set up and how closely it resembles what would be seen on a flight vehicle
2. How loads and/or damage are introduced into the structure under test and the corresponding sensors

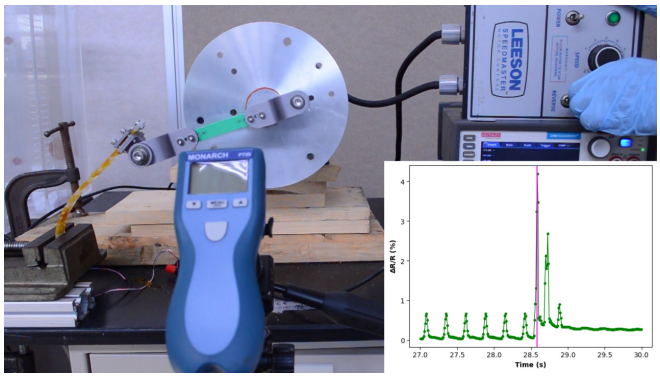

Figure 4. In this benchtop example, the resistance change (inset plot) of CNT sensors was measured during cyclic loading.

3. Aerodynamic and other forces
4. The noise environment around the sensors - includes electromagnetic, acoustic, thermal, etc.
5. The size-scale of the test articles
6. Duration of the tests

Tests on the benchtop and in mechanical load frames as shown in Figures 4 and 5, respectively, are a useful and necessary initial step in the technology evaluation process. Benchtop Tests are relatively simple in set up and quick to turnaround, and various high performance laboratory-scale instruments can be readily deployed. Such testing, however, rarely represents accurate in-flight conditions and is thus rarely relied upon for final conclusion.

For full scale component testing, drop/crash tests such as that shown in Figure 6 can be a highly useful platform to obtain the correct sense of scale and the extreme edge of the working envelope for technology assessment. However, access to drop/crash tests is infrequent, and such tests also typically and intentionally have a fixed loading profile (catastrophic). Damage due to long term cyclic fatigue that would be expected during the operational lifetime of a vehicle and the ability of sensor(s) to detect that damage cannot be investigated via a drop/crash test.

Wind tunnel and flight tests offer the highest fidelity relative to operational flight-like conditions. However, such tests tend to have limitations and restrictions related to facility and/or vehicle safety. The fidelity and difficulty of wind tunnel testing depends to different extents on the risk posture of the facility and the general purpose of the wind tunnel itself (e.g., general use vs. dedicated). For example, a wind tunnel used primarily for academic research (Ref. 9) may accommodate more risky experiments than a large cost-intensive research facility. For multi-objective test flights, the flight itself may be a high-fidelity representation of realistic operational conditions. However, the value of the test results may be limited to parameters tested, e.g., the target subcomponent of interest, the location of the subcomponent in the test vehicle, and

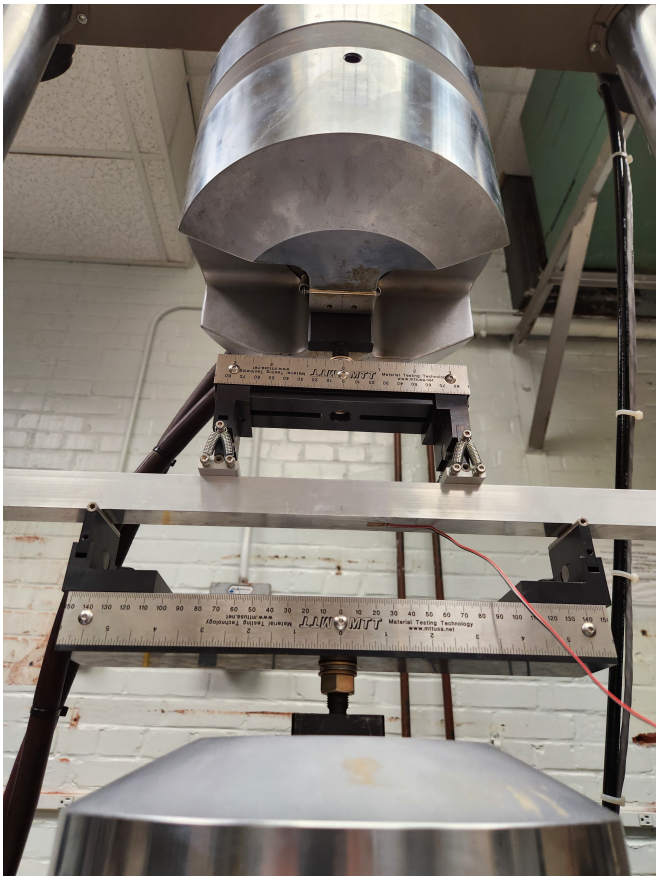

Figure 5. Tests on mechanical load frames are useful for controlling specific test parameters, but like benchtop tests, do not easily provide flight-like configurations/conditions.

the range of conditions experienced by the subcomponent due to its location. This challenge particularly applies in SHM, in which component failure during a flight test may be necessary for adequate validation, but the associated risk to the vehicle may be unacceptable.

Testbeds designed to study particular correlations between various test parameters relevant to specific project objectives are another potentially high fidelity test platform that may not be readily accessible (Refs. 13–15). Again, organization and program risk posture may limit the fidelity of some aspects of the testing. The testbeds may also be a one-off, limiting iterative development.

Purpose built or adapted drones and other aircraft are a platform on which a range of technologies can be tested in environments that can approach final use cases (Ref. 17). There are various levels of difficulty in accessing these platforms that, again, are largely organization/program dependent.

Original equipment manufacturers (OEMs) are the entity which ultimately integrates new technology into application. Not strictly governed by open-ended research and development efforts, OEM testing can provide the most thorough and important test of feasibility in practical application and can accelerate the practical adoption of promising technologies.

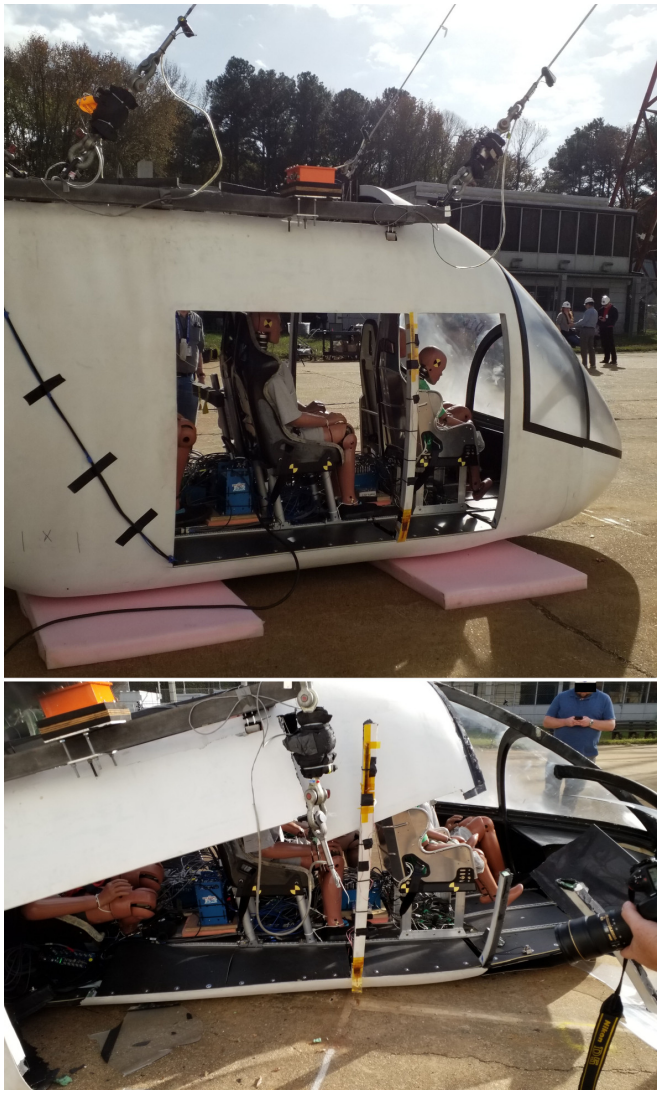

Figure 6. Full scale drop/crash tests provide more realistic representations of flight vehicles but typically only provide the catastrophic load profile and are conducted infrequently.

In the realm of OEMs, the goal is usually to prove that a particular technology is *good enough* to solve a *specific problem*. This approach can streamline decisions on the adoption new technology, overcoming the indecision/lack of proper requirements that may slow the pace of pure research efforts.

Assessing the true feasibility, or otherwise, of sensors enhancing SHM in UAM operations beyond the current practice in other aircraft types will require tests of multiple sensor types monitoring the same structures. In general, the availability of tests dedicated to sensor integration can be a challenge. A multi-use wind tunnel may be difficult to access or restrict damage that can be sustained by the article under test to protect other assets. Similarly, flight articles may be restricted in permissible damage they may sustain during the test or in the exposure to interference that could impact instrumentation. These are important factors to study for the sensor performance in practical use. It is therefore imperative that a suite of different tests and platforms be utilized in order to obtain a more complete understanding of different aspects of the technology use and performance. In addition to benchtop, load frame, and drop/crash tests, a dedicated sensor integration testbed is useful for evaluating and validating a sensor suite dedicated to SHM. The remainder of this report will focus on research utilizing such a testbed.

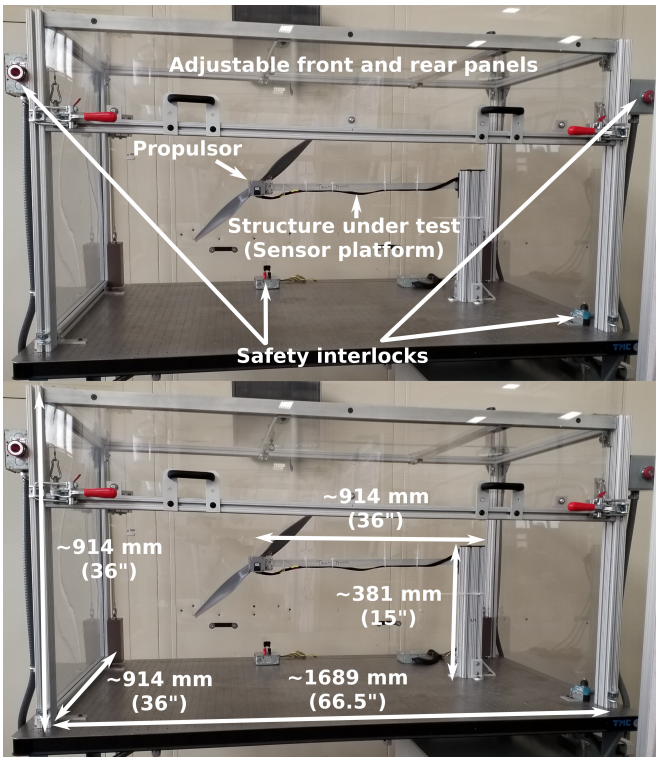

Figure 7. Components and dimensions of the testbed used in this research.

SENSOR INTEGRATION TESTBED

Given the challenges with integrating multiple sensor types and understanding their utility in practical SHM applications, development of a dedicated testbed can be an important testing step. The use of a dedicated testbed does not obviate the need for the other tests described in Figure 3 but complements them. A dedicated testbed can be a step up from benchtop/load frame testing that addresses a range of questions on the path to flight tests. For the work presented here, one such testbed was built and used to assess a combination of several sensor types applied to the same flight-component-like test article. This testbed, which is shown in Figure 7, was aimed at exploring the physical integration of multiple sensor types onto the test component, setting up of the sensor interrogation hardware and software, as well as the overall operations and coverage possible when multiple sensing modalities are involved. Such testing can inform practical sensor selection, deployment, and data acquisition and processing strategies on the path to the envisioned wider use of SHM in airframes.

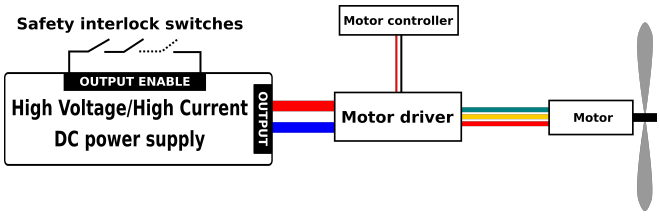

Figure 8. The testbed power circuit consists of a high voltage/high current DC power supply, the motor with controller and driver, and various safety interlocks.

Testbed Components

Key components and dimensions of the testbed are shown in Figure 7. The structural articles under test are housed in an enclosure with fixed side panels and movable front and rear panels. A mounting post is provided on the testbed table for holding the fixed end (hard point) of the structure under test. A propulsor (motor and propeller) that is mounted at the free end of the test article provides the basic loading. Tests showed the need for alternative methods of loading the test article, as described in the *Experimental* section. Several safety interlocks protect the operators during the setting up and running of the tests. A simplified schematic of the testbed power circuit, including the safety interlock switches, is shown in Figure 8.

During test runs, several types of sensors were mounted onto the test article and deployed around the testbed. These included:

Primary (structural) sensor types:

1. Metal foil strain gauge
2. Eddy current
3. Guided wave (acoustic emission and ultrasonic)
4. Fiber optic
5. Carbon nanotube roving strain gauge

Auxiliary sensors:

1. Optical camera
2. Thermal camera (monitoring the propulsor motor)
3. Thermocouples (monitoring the propulsor motor and driver temperature; reference for profiling temperature effects on other sensor types)
4. Global Positioning Satellite (GPS) receiver for the synchronization of data acquisition device clocks
5. Force gauge
6. Digital microscope

The sensors mounted on the initial runs of the testbed all had wires connecting them to the associated data capture instruments. There is work in the literature on various wireless sensor technologies (Refs. 18–20) and for practical SHM applications, eliminating wires will be an important step and therefore future tests should include these technologies.

Modeling

Most as-captured SHM sensor data do not directly provide absolute information about the health of the structure. Additional data processing and interpretation are required to arrive at that information. This interpretation is informed by knowledge about the expected response of the structure in the nominal as well as off-nominal states. For simple geometries this additional information can be obtained from first principles calculations. Validated finite element modeling (FEM) can be used as the structures get more complex. For highly complex structures and sensor deployments, statistical approaches including machine learning (ML) are being adopted to aid data interpretation (Refs. 21–24). Effective use of ML requires large amounts of data from tests that fully cover the expected operational configurations. The data also need to come from tests that simulate the operational conditions and include the responses of the different sensors that may be used. In the current work, and testbed, a simple beam geometry with a hard-mounting point at one end with a point load applied at the other was chosen to simplify the calculations of the expected response.

Metal Foil Strain Gauges

Metal foil strain gauges are ubiquitous and well understood sensor devices that provide local strains. The operation of the strain gauges is based on the resistance change in metallic foils in response to strain. As a device, the strain gauge is primarily a metal alloy trace on a substrate such as polyimide (Kapton) film.

Given a conducting material with resistivity (ρ), length (L) and cross sectional area (A), the resistance (R) is given by: (Ref. 25)

$$R = \rho \frac{L}{A}. \tag{1}$$

Any change in ρ, L and A can lead to a change in the resistance R:

$$R + \Delta R = \rho + \Delta\rho \frac{L + \Delta L}{A + \Delta A}, \tag{2}$$

where delta represents a change in the associated variable. If the resistivity ρ is fixed, by the selection of the sensing material for the strain gauge, as well as controlling for temperature which can change ρ, then any changes in the resistance are directly related to changes in the geometric dimensions of the gauge (ΔL & ΔA), and therefore strain. The design of

the gauges can further be controlled so that changes in R are directly proportional to the linear strain ε ($\varepsilon = \Delta L/L$).

The gauge factor, or strain factor, which is the ratio of the change in resistance to the strain ε, is given by:

$$\text{Gauge factor (GF)} = \frac{\Delta R/R}{\varepsilon}. \tag{3}$$

Typical metal foil strain gauges have a gauge factor $GF \approx 2$.

Eddy Current Sensors

Eddy current testing is a well-established technique for nondestructive evaluation (NDE) of aerospace structures, most commonly applied to metallic components (Refs. 26, 27). Extensively used for the detection of surface breaking fatigue cracks in metals, the method relies upon the coupling of an inspection coil with the part under test via a time-varying magnetic field. An alternating current drives the inspection coil, thereby creating an alternating magnetic field in the vicinity of the coil. A conducting object within this field will develop an induced current flow to oppose the changing magnetic flux as explained by Faraday's law of electromagnetic induction (Ref. 28), with the strength of the induced surface current proportional to the product of the time rate of change of the magnetic flux and the part conductivity. The shielding effect produced by the surface currents leads to an exponential decay of current density with depth into the part under test, given by the skin depth relationship as:

$$J_x = J_0 \exp(-x/\delta), \tag{4}$$

$$\delta = 1/\sqrt{\pi f \mu \sigma}, \tag{5}$$

where J_x is the current density at the surface of the part in amp/(meter)^2, x is the depth into the part in meters, f is the frequency in hertz, μ is the magnetic permeability in henry/meter, and σ is the electrical conductivity in 1/(ohm*meter).

Due to the strong dependence of induced current density on part conductivity, eddy current methods have historically focused on inspection of metallic parts. The high conductivity of these materials leads to typical inspection frequencies in the 10's to 100's of kilohertz and coil diameters on the order of one to a few millimeters. The small diameter of the coils and strong induced current flow in the high conductivity materials leads to excellent sensitivity for surface breaking cracks. As reported in (Ref. 29), fatigue cracks as small as 0.310 mm (0.0122 in.) long × 0.155 mm (0.0061 in.) deep were detected with 90% probability of detection and 95% confidence in 44.26-liter Al 6061-T6 COPV liners. The small footprint of typical eddy current probes leads to a small inspection spot size such that hand or mechanical scanning is required to examine an extended area of a structure. This type of inspection methodology is not well suited for real-time in-situ inspections. An alternate approach applied for SHM using eddy current sensors focuses on crack monitoring at critical locations.

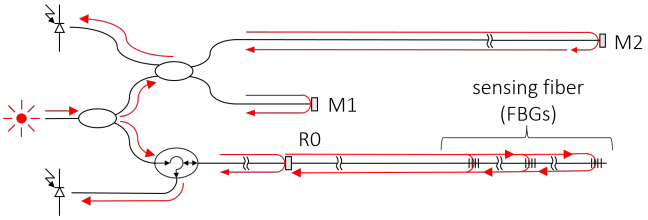

Figure 9. OFDR fiber optic network and sensing fiber.

Here, an isolated single coil or array eddy current probe can be attached or embedded into the structure to monitor for crack growth at the critical location. Some examples of eddy current SHM using this methodology are given in (Refs. 30–33). In this configuration coil size can be adjusted to match the required resolution (spanning ranges from sub-millimeter to several centimeters).

Fiber Optic Sensors

Advantages of fiber optic sensors over electrical counterparts include electromagnetic immunity, lower mass, smaller footprint, and higher bandwidth. Of the many types of fiber optic sensors, the fiber Bragg grating (FBG) continues to be an attractive choice for engineers and researchers. An FBG is a section of optical fiber in which the index of refraction is periodically modulated to induce a reflective response at a resonance, or "Bragg", wavelength (Ref. 34). FBG-based sensing systems typically infer measurements by tracking Bragg wavelength shifts due to fiber-coupled environmental changes such as structural deformation/flexing, temperature, chemical presence, and pressure.

An optical frequency domain reflectometer (OFDR) is capable of simultaneously tracking the Bragg wavelength of hundreds of low-reflectivity ($< 0.1\%$) FBGs in a single sensing fiber, making it a highly-distributed fiber optic sensing platform (Ref. 35). The technology has seen use in several NASA and non-NASA applications and is now available commercially as both a sensing system and a fiber optic component analyzer (Refs. 36, 37). In its simplest form, an OFDR uses a continuous output, high coherence, wavelength-swept source laser to simultaneously drive two fiber optic Michelson interferometers, as shown in Figure 9.

The *reference* interferometer is made up of two differing lengths of fiber, each terminated with a Faraday rotation mirror. The *sensing* interferometer is made up of a partially reflective broadband mirror connected directly to a sensing fiber which holds the sensors of interest (FBGs in this example). Shown schematically in Figure 10, a basic OFDR system configuration consists of a central processing unit (CPU), a fiber network, an external sensing fiber, detection/amplification electronics, and a data acquisition (DAQ) module. The CPU controls the laser, stores data, and provides for digital signal processing (DSP) of the sampled data. The fiber network distributes the laser output to both the internal reference interferometer and the external sensing fiber and directs the optical returns to the detection/amplification electronics. The DAQ

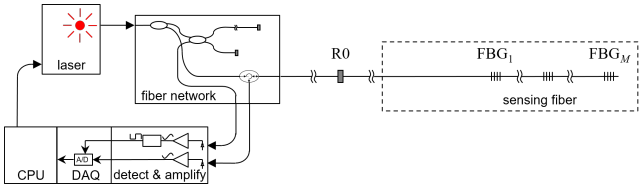

Figure 10. Typical OFDR system architecture.

module performs analog to digital (A/D) sampling of the sensing fiber signal and provides the sampled data to the CPU.

Signal processing in an OFDR begins with sampling the return signal from the sensing fiber during a wavelength sweep of the source laser (Ref. 38). The sampling, or clocking, of the return signal is controlled by the system's reference interferometer, giving a *raw data set* with a linear basis in wavenumber. Fourier transforming the raw data set gives the *spatial set*, in which gratings are separated by their unique distance from the reference reflector. To isolate the response of a specific FBG, the spatial set is windowed, or band pass filtered, around the grating of interest before being inverse Fourier transformed back to the wavenumber domain to reveal the reflection response, or reflection spectrum, of the grating. Center reflection wavelength is determined using a peak detection algorithm such as thresholding and center-of-mass calculation on the grating reflection spectrum. Strain is determined by tracking the wavelength shift from a zero-strain wavelength value and applying

$$\varepsilon = \frac{\Delta\lambda_B}{\lambda_{B_0}(1-p_e)}, \tag{6}$$

where ε is the axial strain within the FBG, $\Delta\lambda_B$ is the spectral shift of the Bragg wavelength, λ_{B_0} is the Bragg wavelength at zero strain, p_e is the effective strain-optic constant, and the gauge factor of the FBG strain gauge is $(1-p_e)$ (Ref. 39).

Guided Wave Sensing

This effort employs the guided wave methodologies of acoustic emission (AE) sensing and guided wave ultrasonic transmission (UT). Guided wave sensing makes use of elastodynamic waves in the frequency range of 50 kHz to 2 MHz propagating through a structure longitudinally (parallel to the surface plane). Most structures are made of elements such as plates and beams, the geometry of which defines the capable wave propagation modes for specific frequency ranges (Ref. 40). Initial conditions and material anisotropy create a variety of potential modes of propagation determined by characteristics such as the direction of the microstructural particle motion versus the macrostructural direction of the wave propagation. Changes in mechanical properties via damage or processing inhomogeneity, further affects the propagating modes. This allows the potential to characterize those changes and the health of the structure.

Acoustic Emission (AE) in a structure under mechanical load is created by rapid release of stored energy on a microstructural scale via dislocation motion or crack initiation/growth. Typically, the predominant AE energy is propagated through the structure via shear modes. The wave energy is captured by sensors (typically piezoelectric transducers) secured to the surface structure at locations remote from the event epicenter. AE is considered to be a guided wave technique due to the reliance on elastodynamic wave propagation to transfer energy from the source to the sensor.

Guided wave UT utilizes a controlled energy source, such as a piezoelectric transducer, to induce elastodynamic waves into a structure. The injected energy propagates away from the source, longitudinally through the structure, and impacts various in-homogeneous features which induce reflection and/or mode conversion. One or more receiver transducers, and in some applications, the source transducer, collect the reflected/transmitted wave energy for analysis to detect possible flaw development and location.

With both AE and guided wave UT utilizing the ultrasonic frequency regime, there is significant interest in developing techniques to combine both approaches (Ref. 42). Described in more detail in the Experimental section, the instrumentation used in this effort combines AE capture with a pitch-catch guided wave UT architecture in which repeatable, consistent guided waves are induced via a dedicated pulsing transducer and recorded by the AE capture transducer. The proposed scheme monitors AE data to detect damage events (cracking) and analyzes the UT guided wave data to detect energy changes due to flaw development (crack growth).

Carbon Nanotube Roving Sensors

A more experimental sensor technology, carbon nanotube (CNT) roving sensors, were also used in the current work. CNTs are nanometer sized cylindrical molecules with mechanical, electrical and thermal properties that have attracted interest for a range of applications in many different domains since their discovery. The availability of macroscopic assemblages (Ref. 43) of the nanotubes has attracted use in applications that range from reinforcements for structural aerospace composites (Ref. 44) to wearable textiles (Ref. 45) and anti-icing/de-icing systems (Ref. 46). CNTs have been explored for various sensing applications (Refs. 47–49). While there have been efforts on using the individual nanotubes, CNT powders dispersed in polymer matrices or CNT yarns as strain sensors, the current work focused on utilizing the electrical properties of CNT rovings, a macroscopic assemblage of nanotubes as the sensing element. The CNT rovings shown schematically in Figure 11 are a loose network of interconnected nanotube bundles. Changes in those network connections, such as those induced by strain, lead to changes in the electrical resistance. It is this change in resistance that is being used for sensing. The nanotube network responds linearly to small strains, similar to metal foil gauges, but large strains can induce plastic deformation and thus a memory effect for extreme excursions, similar to other "fuse-style" sensors. Plastic deformation of the roving from the extreme excursions causes a step change in the baseline resistance into a linear region

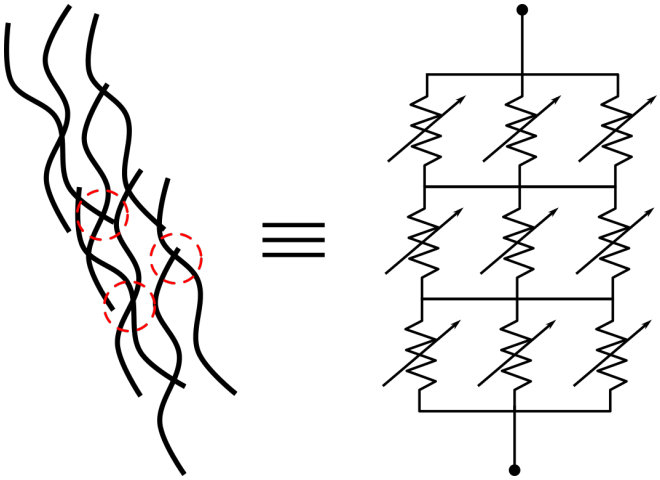

Figure 11. Carbon nanotube rovings are a loose network of interconnected CNT bundles (left) that can assemble to function as an equivalent circuit (right).

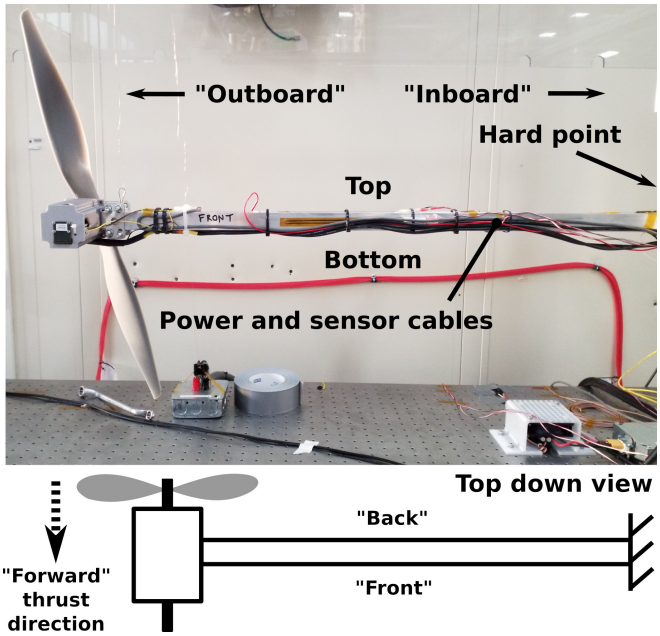

Figure 12. Directional orientation of the test beam are as follows: Inboard points from the motor toward the hard point, Outboard points from the hard point toward the motor, and the thrust direction is toward the view position, or out from the page.

with the new baseline. This potentially makes them "reset-table/reusable fuse-style" sensors. It is this combination of linear and non-linear response regimes as well as the large strains and high cycle life that they are able to withstand that could make the rovings an interesting sensor technology. This work focused on testing a particular method of fabricating de-ployable sensor devices from the CNT rovings.

EXPERIMENTAL

Testbed Specifications

An Ametek XG 30-50[1] 1500 W (0 to 30 V and up to 50 A) direct current (DC) supply was used as the high voltage/high current source for the propulsor in an implementation of the circuit shown schematically in Figure 8. The DC source provided power to a pulse width modulation (PWM) driver that in turn supplied the motor coils. A Phoenix Edge 50 A electronic speed controller (ESC) was used as the motor driver with the motor speed governed by settings to this controller. Speed was manually set using a Turnigy 7-in-1 Mega Meter Battery Checker/Watt Meter/Servo Tester. A US5881 Hall-effect sensor mounted at the propulsor motor coils was used for speed measurements. An NI USB-6361 A/D and a custom coded LabVIEW application captured the Hall-effect sensor data. Voltages and currents delivered by the DC power supply were also captured using a custom coded LabVIEW application.

Test Beam Configuration

Reference directions of the test beam are shown in Figure 12. "Front" and "Back" are in the coordinate frame of the testbed housing. "Inboard" and "Outboard" are in the coordinate frame of the test arm with the hard point as the origin. Power cables for the propulsor and wiring for sensors are also shown in the figure.

The mounting locations for the sensors on the test beam are shown in Figure 13. The metal foil strain gauges (1a and 1b) and eddy current coils (2a and 2b) were mounted near the hard point. The pair of metal foil gauges were placed on orthogonal faces of the beam to measure strains in-line with and perpendicular to the propulsor thrust. The fiber optic sensors (3) stretched from near the hard point outboard to near the propulsor. One of the guided wave transducers was positioned near the hard point (4a/4a*) and the other was mounted further outboard (4b), ensuring there was a transducer either side of the test beam notch location. In the figure, the location of the cut is marked as (X* and X) indicating before and after it was made. The CNT roving sensors (5a and 5b) were mounted in the remaining real estate, further outboard on the beam. Similar to the metal foil gauges, the CNT roving gauges were also mounted on orthogonal faces of the beam.

For the secondary test campaign, described below in the Testing Sequence subsection, an additional CNT roving sensor was mounted inboard, closer to the hard point. The mounting location of the additional CNT sensor (5c) is shown in Figure 14. The temperature response of the CNT sensors (5a and 5c) was measured with the set of thermocouples (6a and 6b) shown in the bottom image in Figure 14 acting as the references.

[1] Specific vendor and manufacturer names are explicitly mentioned only to accurately describe the test hardware. The use of vendor and manufacturer names does not imply an endorsement by the U.S. Government nor does it imply that the specified equipment is the best available.

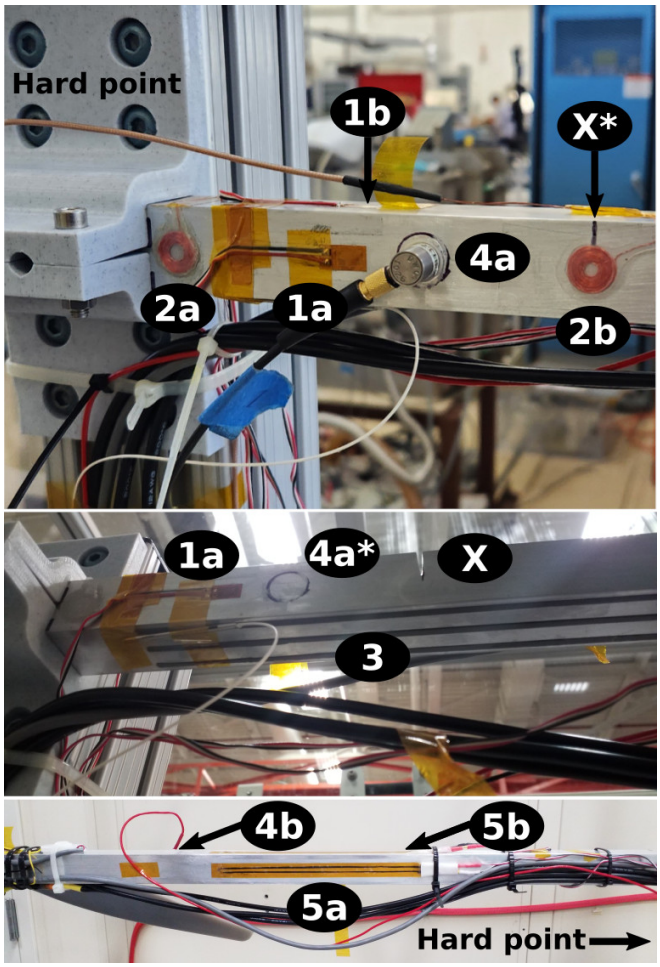

Figure 13. Sensor types and locations detailed are: metal foil strain gauges (1a and 1b), eddy current coils (2a and 2b), fiber optic sensors (3), guided wave transducers (4a, 4a*, 4b), and CNT roving sensors (5a and 5b). The notch location, before and after notching, is labeled X* and X, respectively. *'s indicate locations for components/features that were not in place at the time of image capture.

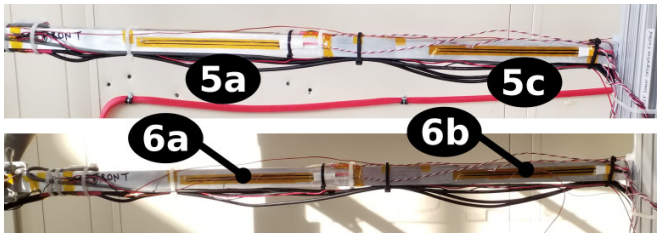

Figure 14. An additional CNT roving sensor was mounted inboard for the secondary test campaign (5c). CNT temperature referencing at locations 5a and 5c was monitored with thermocouples (6a and 6b).

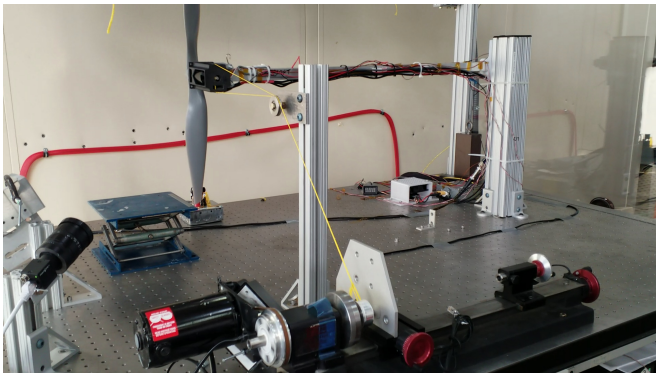

Figure 15. A motor driven cam connected via cable to the beam provides quicker, higher load fatigue cycling of the beam than propulsor loading.

Control and Data Capture

Several computers running Debian Linux and Microsoft Windows as well as custom standalone DAQs were used for data capture. The Linux and Windows computers ran custom written Python and LabVIEW applications and vendor supplied software specific instruments as available. The testbed control computers and instrumentation were connected over a high speed dedicated local area network (LAN). The LAN was set up using a Linksys EA6100 AC1200 Dual-Band WiFi Router in Ethernet only mode (wireless radios turned off) as the Dynamic Host Configuration Protocol (DHCP) server with its Ethernet ports providing connection points. A NETGEAR XS708E 8-Port 10-Gigabit Ethernet Plus Switch and a NETGEAR ProSAFE FS105 Fast Ethernet Switch were used to expand the available connection points. Time synchronization for the networked computers, which were isolated from the internet for the tests, was provided by a Netburner PK70 EX NTP Network Time Server on the same LAN. The PK70 uses the Network Time Protocol (NTP) to enable host devices on the network to maintain accurate time. The PK70 in turn receives its time information from GPS satellites.

Test Beam Loading

During "regular" test runs, the load was applied via the propulsor at the end of the structural test beam. Varying the rotational speed of the propulsor varied the applied load. Prior calibration using a force meter had established the load/speed profile of the test setup.

To provide higher fatigue cycling and accelerate the growth of the crack in the notch cut into the test beam, a cam driven setup was used. This setup, shown in Figure 15, was used for approximately 11,000 cycles before the test beam was again loaded using the propeller. The headstock motor on a Sherline tabletop lathe was used to drive the cam.

During the secondary test campaign the test beam was also deflected by hand to compare the response of the CNT roving sensors and the metal foil gauges to sharp taps. The magni-

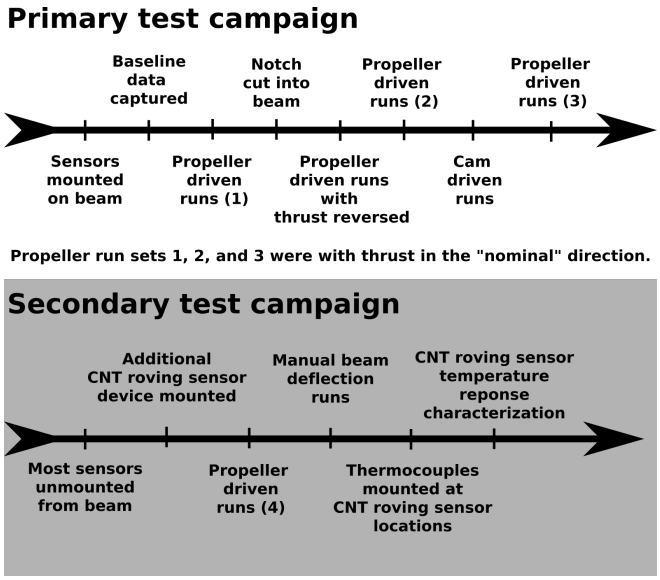

Figure 16. Data from all beam sensors were recorded during the primary test sequence and a secondary test sequence focused primarily on the response of CNT roving sensors.

tude of the deflection was guided by the strain measured by the metal foil strain gauges.

Testing Sequence

The sequencing of the sensor testing done on the testbed is shown Figure 16. Two test campaigns were run, a "primary" test campaign involving multiple sensor types and then a "secondary" test campaign to further characterize the response of the experimental CNT roving sensor devices. With all sensors mounted and the test beam secured in the testbed, baseline sensor data were acquired. Baselining was followed by a series of runs in which the beam was driven by the propeller. A notch was then cut into the beam and another series of testing followed. This series included more propeller driven runs and a set of runs in which a cam was used to load the beam and accelerate the growth of a crack from the notch. Following this series of tests, most sensors were removed from the test beam and an additional CNT roving sensor mounted for the secondary test campaign. In this campaign, a series of tests were conducted gathering data from the CNT roving sensors mounted "inboard" and "outboard" on the "front" face of the test arm. The testing concluded with profiling of the temperature response of the front facing CNT roving sensors.

Metal Foil Strain Gauges

A pair of Micro-Measurements CEA-13-250UW-350/P2 (part no. MMF017732) strain gauges was mounted on the test beam orthogonal to each other and near the hard point as shown in Figure 13. Gauges were mounted using Micro-Measurements M-Bond 200 strain gauge adhesive. Data from the strain gauges was captured using an NI-9236 interface module mounted in an NI cDAQ-9178 CompactDAQ chassis. The same custom built LabVIEW-based application used to capture the motor speed data also recorded the strain data.

Eddy Current Sensors

Single layer, pancake, eddy current coils were used to monitor crack growth in the area of the notch on the aluminum beam of the sensor testbed. The coils were wound using 36 AWG copper magnet wire. Winding was performed around a 3.175 mm (1/8 in.) diameter dowel pin. Approximately 32 turns of the 0.127 mm (0.005 in.) diameter wire were wound in a single layer resulting in a flat coil with an inside diameter of 3.175 mm (1/8 in.) and outside diameter near 12.7 mm (½ in.). Two coils were mounted on the beam, one directly under the notch and a second close to the hard mount. The coil at the notch was taped in place to allow easy removal and remounting between fatigue runs such that magnified visual and scanned eddy current array inspections could be performed to document crack growth between test runs. The coil near the hard mount was bonded to the beam. A picture of mounted coils is shown in Figure 13. All eddy current Lissajous responses reported here were acquired with the coil at the notch location.

Each inspection coil was paired with a matched coil outside of the testing zone. The matched pairs were wired to a Zetec Miz-27 eddy current instrument operating at 250 kHz. The eddy current equipment measured the change in the real and imaginary components of the electrical impedance of the coils and displayed results as a Lissajous curve in a phase rotated complex plane at a data acquisition rate of 200 samples/sec. The phase angle of the change in impedance was rotated to project the lift-off response to the negative horizontal direction. A data set acquired while manually scanning the sensing coil across the notch in the beam is displayed in Figure 17. The lift-off response is along the negative horizontal direction (as expected) while the notch response occurs at approximately 155 degrees. A gain of 30 dB was used for this calibration data.

Fiber Optic Sensors

The sensing fiber, FBGS part no. AGF-LBL-1550-125 (Ref. 50), contains FBG sensors 9 mm (0.35 in.) in length, spaced 1 cm (0.39 in.) center-to-center, and was bonded along the underside of the beam 3.175 mm (0.125 in.) from the edge over a distance of 60 cm (∼24 in.) using Henkel Loctite EA 9394 AERO adhesive. To connect to the inline reflector and ultimately to the OFDR interrogator, the sensing fiber was fusion spliced to a standard 900 micron-buffered SMF-28 fiber terminated with an FC/APC connector. The FBG sensing fiber location on the test beam is shown in Figure 13.

The OFDR system used is custom assembled and housed in an NI PXIE-1065 chassis. The system laser is a New Focus TLM-8700-H-CL. Both the reference leg detector and the sensing leg detector are Thorlabs model PDB460C. Two NI DAQ cards, model PXI-6115, control the system timing and

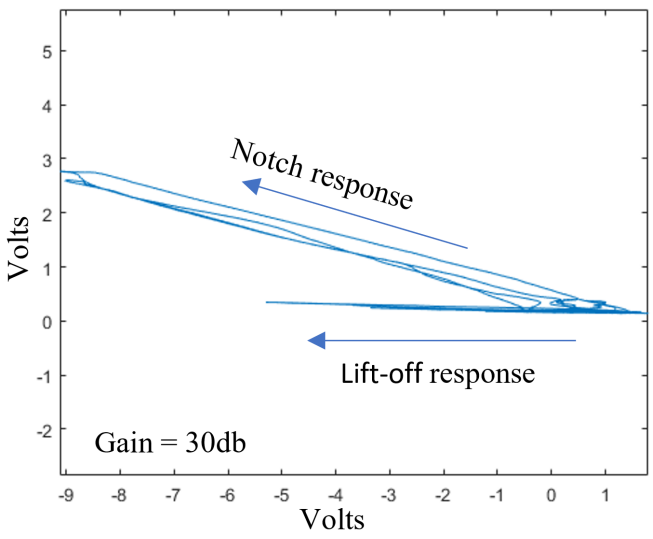

Figure 17. Eddy current response is recorded during hand scanning of the inspection coil across the notch in the aluminum beam. Units of X and Y axes are in volts and are proportional to the impedance change along the corresponding axes.

Figure 18. The palm-sized spotWave acoustic emission system was configured as both an AE listener and a guided wave UT interrogator.

raw data sampling. The system control and processing CPU is an NI PXIE-8135 embedded controller. The fiber network is made of standard communications grade components (SMF-28 equivalent) and contains a 30.182 m (∼99 ft) long reference leg of standard SMF-28 fiber with two Faraday rotator mirrors serving as the reference interferometer reflectors. The inline broadband reflector is a titanium-oxide partial reflector (30%) manufactured by AC Photonics. FC/APC connectors are used where necessary (from the laser to the fiber network, for example).

Guided Wave Sensors

The spotWave, an AE system from Vallen Systeme GmbH, is shown in Figure 18. This-palm sized instrument (∼50.8 x 76.2 x 12.7 mm^3) (∼2 x 3 x 0.5 in.^{3}) is designed for AE monitoring of hotspots of potential or existing fatigue damage in a structure. The system collects, reduces, and stores characteristic features of detected AE waveforms from a single transducer mounted to a structural surface. To ensure operational integrity during long-duration, unattended data collection, the spotWave has a pulsing output channel capable of periodically generating an *artificial* AE signal on a second transducer mounted on the same surface as, but at some distance away from, the sensing transducer. The unit uses the artificial AE signal as a check of the functionality of the AE sensing channel. The signal to the pulsing transducer is a square wave with adjustable interval and rise/fall times. The functionality of the integrity check coupling between the AE sensing and pulsing transducers makes up a psuedo pitch-catch guided wave UT interrogation of the structural material between the two.

The piezoelectric AE/UT transducer pair was mounted on the front face (side of highest tensile stress) of the beam. The AE sensing transducer is a Digital Wave B1025 (100kHz - 3MHz bandwidth, ∼9 mm (0.365 in.) dia.). The UT generation transducer is a Physical Acoustics U30S (250 kHz center freq., ∼9 mm (0.365 in.) dia.). The center frequency (250 kHz) of the U30S transducer is adequately close to the 200 kHz frequency of the peak energy carrier as determined by pre-test evaluation of the beam propagation characteristics.

The transducers were attached to the beam surface with a combination of aluminum tape and adhesive. At the points of attachment, aluminum adhesive tape pads (Nashua 324A Cold Weather) are first placed directly to the beam surface (adhesive-side to surface). Each transducer was then bonded to the non-adhesive side of its respective pad (Lord 403/19 Acrylic adhesive). This combination of tape and adhesive does not adversely affect acoustic coupling, and allows for rapid cure (2-4 minutes) without brittleness and relatively easy detachment while avoiding damage to the substrate. The AE transducer was mounted about 127 mm (5 in.) from the notch on the Inboard side of the notch to capture AE originating from crack growth (Figure 13). The pulsed transducer was mounted 559 mm (22 in.) Outboard of the notch near the motor. The transducer placements enable the AE transducer to capture unimpeded crack-generated AE signals and capture the pulser-generated guided waves traveling past the growing crack.

Carbon Nanotube Roving Sensors

The CNT roving sensors were custom fabricated for the testing reported here. Note that the CNT roving sensor experiments were intended not as a test of the intrinsic sensing capability of the sensor itself but, more specifically, to test a quick fabrication method for sensor *devices* that could be easily handled and mounted in the field. Similarly fabricated devices were also deployed during a drop test depicted in Figure 6.

More details on the fabrication of the devices are given in the Appendix. The size of the sensors was chosen to give a resistance of $\sim 100\ \Omega$ and to explore the effect of measuring strains over a larger area. The CNT roving sensors were mounted on the test beam using M-Bond 200 adhesive and located as shown in Figure 13 and Figure 14. Two Keithley DMM7510 7½ Digit Digital Sampling Multimeters (DMMs) were used to gather data. The DMM integration times, in Number of Power Line Cycles (NPLC), were set to 0.0005 NPLC for all of the primary test campaign (Figure 16) and between 0.05 NPLC and 0.0005 NPLC during the secondary test campaign with 1 NPLC corresponding to a time of 16.67 ms. For the temperature response characterizations the integration time was set to 0.005 NPLC. The sensors were read by a custom Python-based application. The application used the LAN and TSP-Link expansion interfaces to communicate with the instruments (Ref. 51). The custom software was run on a Debian Linux platform to enable a real-time data reading rate of up to ~ 200 samples per second over long measurement runs with minimal operating system overhead.

Auxiliary Sensors

In addition to the structural sensors on the test beam, several sensors were mounted around the testbed. A Teledyne Flir BlackFly 2.3 MP Color GigE PoE (Sony Pregius IMX249) Machine Vision Camera with a Fujinon CF12.5HA-1 1" 12.5 mm Industrial Manual Lens for C-Mount Machine Vision Cameras was used for capturing optical imagery. FlyCapture software (Flir) was used to communicate with the camera over the Ethernet network. A Sierra-Olympic long wavelength infrared (LWIR) camera, the Viento-G Performance LWIR with Gig-E Vision, was used to capture infrared (IR) images. Viento GUI software (Sierra-Olympic) was used for the IR imaging. Type K thermocouples were mounted on the motor housing and the motor driving ESC. Thermocouple data was captured using a Measurement Computing Corporation (MCC) USB-TC DAQ. Custom LabVIEW-based software was used to communicate with the DAQ over USB. A thermistor was mounted adjacent to the motor coils and its data collected using a Keithley 2700 Multimeter/Data Acquisition/Switch System. A Dino-Lite AM73915MZT (R10) digital microscope was used to image the growth of the crack in between fatiguing cycles. DinoCapture imaging software was used with the microscope. A Mark-10 force gauge was used to measure the load needed to deflect the test beam. Loads were read directly from the gauge display. Reference measurements during the profiling of the CNT roving sensor temperature response were made using the Type K thermocouples (Nickel-Chromium / Nickel-Alumel) with a Steinel HL 1920 E heat gun providing heat.

Modeling Expected Responses

To estimate the behavior of the beam under loading and to determine a useful location and size of the eventual notching

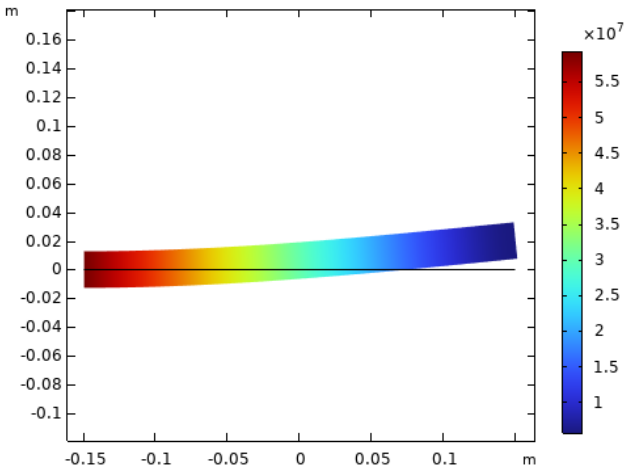

Figure 19. Modeling gives simulated stress and displacement of the undamaged test beam under a 44.48 N (10 lbf) forward end load. The color bar unit is Pascal (N/m^2).

of the test beam, modeling of the expected response was performed using COMSOL Multiphysics. The aluminum 6063-T83 beam was modeled as a hollow structural section with one fixed end and one end under point loading. Details for the modeling were:

- Beam dimensions: 25.4 mm (1 in.) square perimeter with 1.588 mm (0.0625 in.) wall thickness and 0.3 m (11.8 in.) long
- Beam Young's Modulus: 69 GPa ($\sim 1 \times 10^7$ psi)
- End load: 22.68 kg (50 lbs)
- Damaged section: 5 mm (0.20 in.) long, 100 mm (3.98 in.) from the fixed end with a modulus of 6 GPa ($\sim 1 \times 10^6$ psi)

The stresses applied to the beam during the loading are shown in Figure 19.

The structural model of the test beam was further refined to examine stresses near a crack-like defect in the component. The results from this simulation were used to determine the placement and dimensions of the notch in the test beam. For the refined modeling, COMSOL Solid Mechanics Linear Elastic Solver was used. The beam was modeled as Aluminum 6061-T6, 762 mm (30 in.) long, 25.4 mm (1 in.) square perimeter with 1.588 mm (0.0625 in.) wall thickness. A notch was placed 127 mm (5 in.) from the fixed end as a square cut protruding through ½ of the top and rear surfaces of the beam with a width of 0.5 mm (0.02 in.). The FEM used had 133260 elements and 7.9989×10^5 degrees of freedom. A load of 44.48 N (10 lbf) was placed on the free end of the beam in the forward direction.

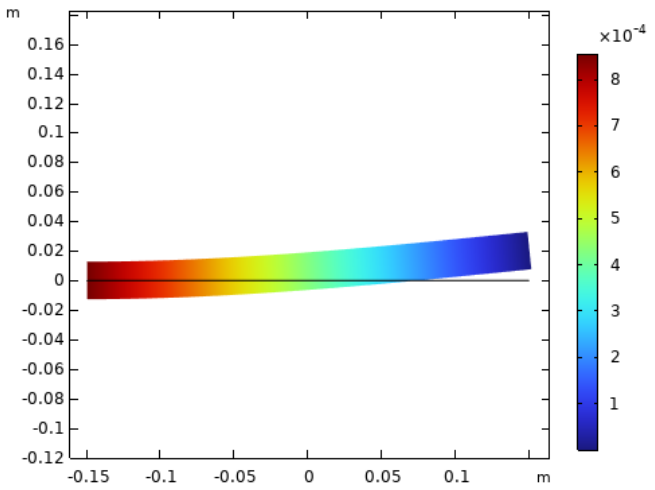

Figure 20. Modeling gives simulated normal strain and displacement of the undamaged test beam under a 44.48 N (10 lbf) forward end load. The color bar is a dimensionless strain value.

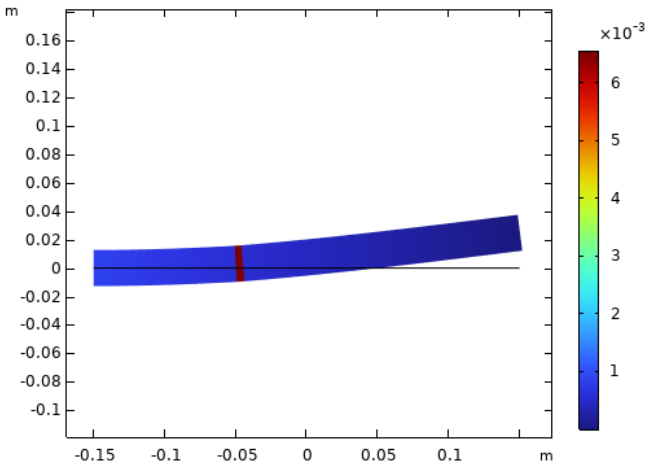

Figure 21. Modeling gives simulated normal strain and displacement of the damaged test beam under a 44.48 N (10 lbf) forward end load. The color bar is a dimensionless strain value.

RESULTS

Modeled Responses

The expected strains from the initial modeling of the undamaged and damaged beams are shown in Figure 20 and Figure 21. These strains are for loading provided by the propeller. For the undamaged beam, there is a smooth gradient of strains moving outboard from the hard point. The data for the damaged beam does not show the same gradient on the scale used. Instead, there is a dominant region of high strain at the damage location.

Line graphs of the maximum normal strain and the displacement magnitude are shown in Figure 22. Beginning at the hard point, arc length =0, the damaged and undamaged beam responses overlap until the location of the damage is encountered at arc length = 0.1 m. At the damage location the strain goes off-scale and the displacement diverges from the undamaged model with increasing magnitude toward the loaded end.

Results from the FE model of the test beam showing the stresses induced from propulsor loading are shown in Figure 23. The model shows that the forces generated by the spinning propeller can create stresses near the flaw that are high enough to induce fatigue crack growth. A line plot of the stresses along the y axis 0.5 mm (0.02 in.) below the crack-like flaw is shown in Figure 24. The model shows stresses near the flaw exceed 150 MPa ($\sim$ 22000 psi). These simulation results were used to guide the placement and depth of the notch cut during testing.

Metal Foil Strain Gauge Response

Typical responses from the pair of metal foil strain gauges during a run where loading was induced by the propulsor are shown in Figure 25. In the figure, the corresponding motor

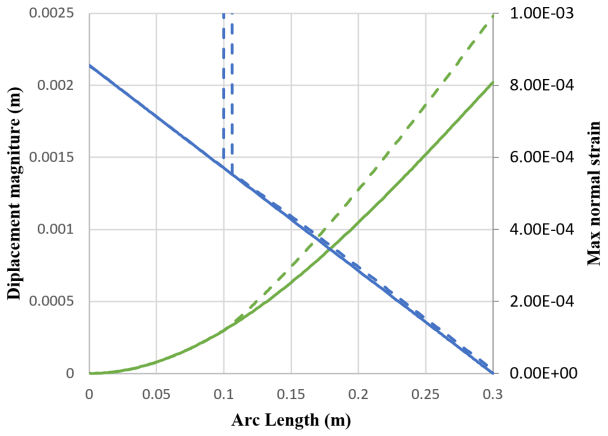

Figure 22. Simulated displacement (green) and maximum strain (blue) for the undamaged (solid) and damaged (dashed) beams.

speed in revolutions per minute (RPM) is also plotted. Both the gauge mounted on the top of the beam (orthogonal to the thrust direction) as well as that on the "back" of the beam (Figure 12) and in-line with the thrust showed clear responses when load was applied by increasing the motor speed. The gauge mounted in-line with the thrust showed a stronger response that is proportional to the expected thrust given the motor speed setting.

Eddy Current Sensor Response

During initial testing with propeller loading very little vertical movement of the impedance of the test coil was observed and no clear sign of crack growth was evident with either magnified visual or eddy current array scanning. While peak strains of over 500 microstrain were recorded by attached metal foil strain gauges, peak to peak strains during the test run were

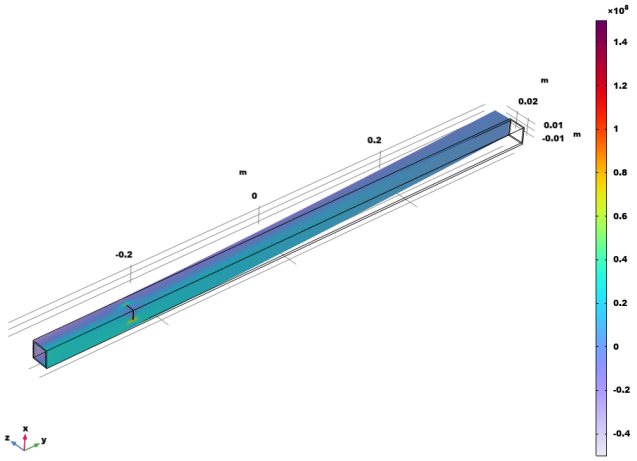

Figure 23. Modeling gives the simulated stress tensor for the notched beam. The color bar unit is Pascal (N/m^2).

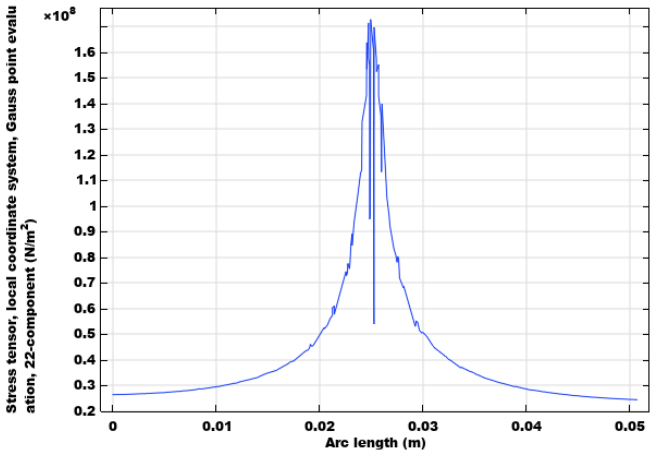

Figure 24. Modeling gives the simulated stress along the long axis of the beam below the notch.

small. In order to increase fatigue, a cam loading system was instrumented on the beam (Figure 15). With this system a cyclic loading of the beam between 100 and 700 microstrain at a frequency of 5 Hz was achieved. The fatigue loading was continued for approximately 35 minutes, during which significant change in the impedance of the eddy current coil near the notch was observed, and is documented in Figure 26. After the test was stopped eddy current array imaging and magnified visual inspections of the notch area were performed and verified fatigue crack growth. A crack extension of 1.9 mm (0.075 in.) beyond the notched region was measured. Eddy current C-scan images of the notch location before and after the run were acquired with a flexible eddy current array (Ref. 33) and are displayed in Figure 27.

Two additional 5-minute cam loading runs at the strain spectrum documented above were performed following the longer crack initiation run. During the first 5 minute run an increase in the eddy current response of 3.5 V was recorded at a phase angle consistent with crack growth. During the

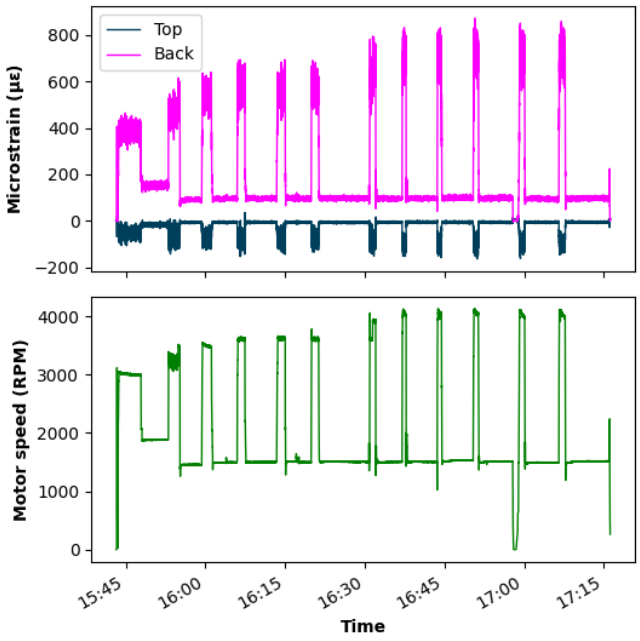

Figure 25. Responses of the metal foil gauges during a typical propeller driven run.

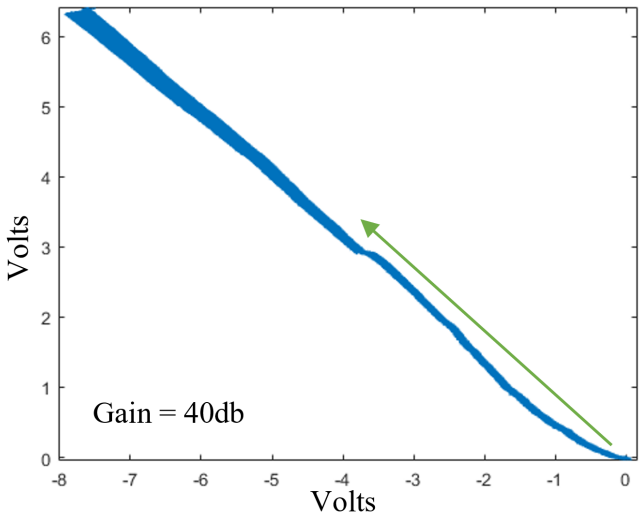

Figure 26. Eddy current response was recorded during first cam loading run. Units of X and Y axes are in volts and are proportional to the impedance change along the corresponding axes.

second 5 minute run the increase in signal was 5.1 V. Magnified optical measurements between runs measured the corresponding crack growths as 0.17 mm (0.0067 in.) and 0.52 mm (0.020 in.). A final 10-minute fatigue run with cam loading at the spectrum described above was performed. Due to the increasing crack growth rate, the gain of the in-situ eddy current measurements were reduced by 6 dB to 34 dB. The magnitude of the eddy current response during this run was 5.4 V at 34 dB gain. The eddy current response during this run is

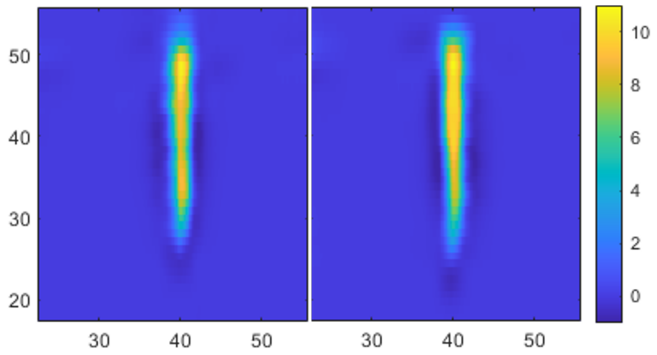

Figure 27. Eddy current array C-scan images of notched area were captured before (left) and after (right) crack initiation and growth. Image axes are in mm. Color map unit is volts.

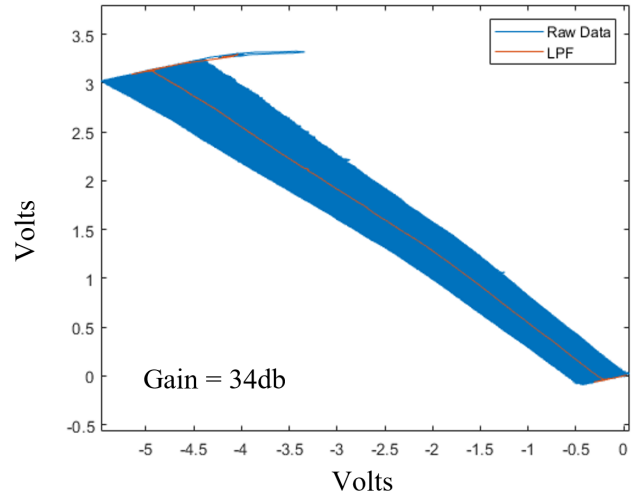

Figure 28. Eddy current response was recorded during final run of cam loading. Units of X and Y axes are in volts and are proportional to the impedance change along the corresponding axes.

displayed in Figure 28. The large horizontal response is due to the increase lift-off of the coil caused by the bending of the arm. As the coil is only taped to the surface, an increase in lift-off occurs during each unloading cycle of the arm. The data acquisition rate of 200 Hz is fast enough to monitor these inter-cycle changes in impedance. The application of a 2 Hz low pass filter (LPF) eliminates the inter-cycle changes and results in the red curve in Figure 28, highlighting the crack growth. An increase in crack length of 1.5 mm (0.059 in.) was measured via magnified optical measurements following the run.

Following the cam loading runs the testbed set-up was returned to propeller loading to test the capabilities of the measurement in a more flight like scenario. During this run motor speed was ramped between approximately 500 and 3500 RPM at a period of approximately 0.3 Hz. The strain spectrum was measured at between 75 and 550 microstrain. Approximately

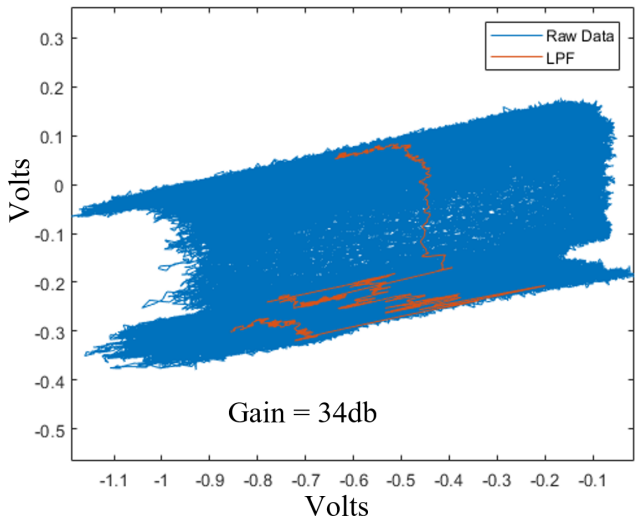

Figure 29. Eddy current response was recorded during simulated flight ramps. Units of X and Y axes are in volts and are proportional to the impedance change along the corresponding axes.

425 cycles were acquired during the run. The eddy current response during this run is displayed in Figure 29. A clear propagation of the signal in the crack-like direction was recorded. The increase in signal at 34 dB gain was approximately 0.4 V and the measured crack growth was 0.27 mm (0.011 in.).

Fiber Optic Sensor Response

The strain changes along the underside of the beam, as measured by the fiber optic strain gauges at various stages of crack propagation, are plotted in Figure 30. A clear progression can be seen in the response from the baseline test (no cut) to when the crack is growing. In addition to the contributions of the applied load, temperature changes and any shift in the propulsor power cables (Figure 12) are expected to also affect the sensor data, making the immediate interpretation of the absolute values difficult.

Guided Wave Sensing Response

Unfortunately, AE events were detected that were not due to the UT pulses in the no-damage baseline runs with the propeller running at the highest speeds. These events were not cracking of the beam since this data was taken before adding stress concentration at the notch. This result suggests acoustics originating from the clamped end fixation, the stand, the motor mount, or the motor itself make up the captured AE events.

The AE system proved more useful in the pitch-catch guided wave UT configuration. Upon pulsing the UT generating transducer, the AE capture transducer picks up the UT energy as a single AE event after propagation through the beam. Changes in the UT energy due to beam notching and crack

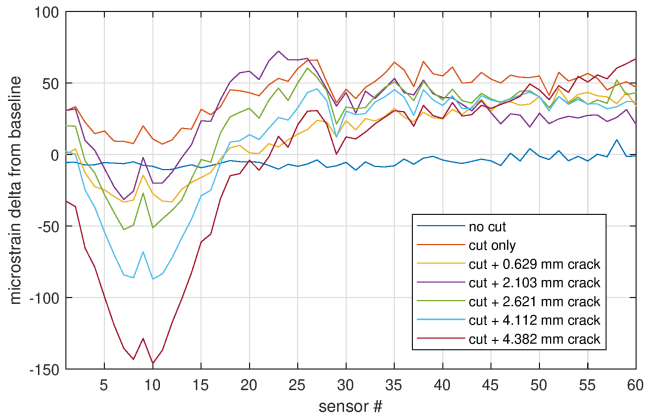

Figure 30. Strain change from baseline (no cut) as measured by FBG strain sensors.

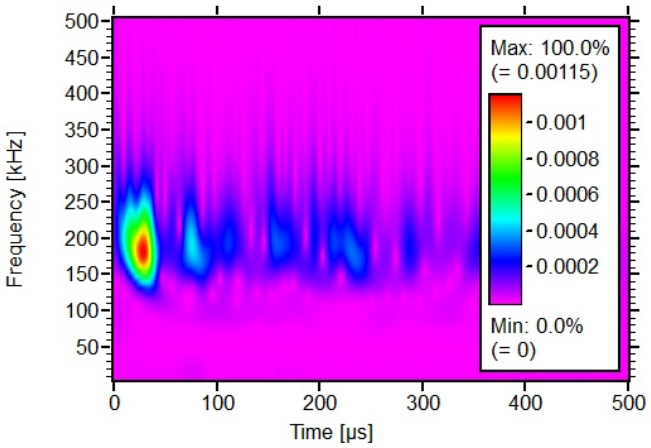

Figure 31. Wavelet transform of UT pulse before notching the test beam shows significant energy concentration of coherent wave propagation around 50 μs.

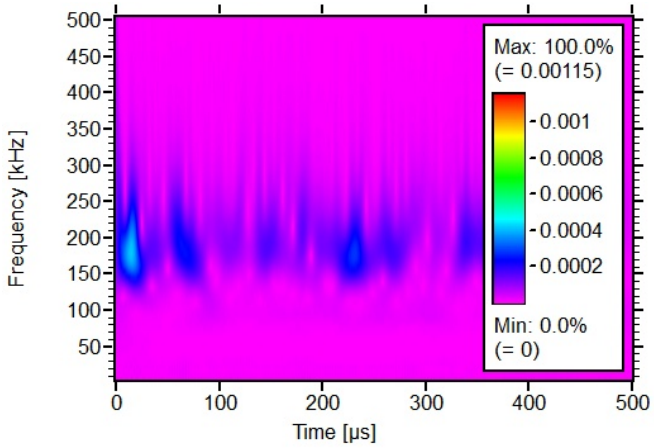

Figure 32. Wavelet transform of UT pulse after notching the beam and before fatigue cycling shows significant changes in the early wave propagation.

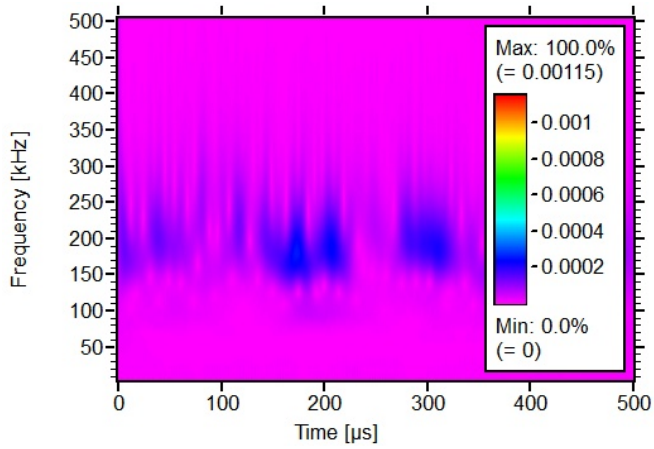

Figure 33. Wavelet transform of UT pulse after mechanical fatigue shows significant reduction in wave propagation throughout the capture time window.

propagation are analyzed using wavelet transform into the frequency vs time domain. The wavelet transform result of a single UT pulse/AE capture signal recorded during undamaged beam fatigue cycling is shown in Figure 31. Note the higher energy of coherent wave propagation early in the signal around 50 μs.

The wavelet transform result of the UT signal just after notching the beam (no fatigue cycling) is shown in Figure 32. Note the significant loss of energy or coherence in the early wave propagation and significant change in the clusters of energy around 200 μs.

The change in wave propagation after the cam-loading fatigue cycling, which generated significant crack growth, are seen in the UT wavelet transform in Figure 33. The early wave propagation is barely above noise level with significant reduction in the remainder of the event, especially when compared to the baseline data shown in Figure 31.

Carbon Nanotube Roving Sensor Response

The typical as-measured responses of the CNT roving sensors are shown in Figure 34. The top plot is from data gathered during runs with cam-loading and using sensors mounted on the front and top of the test beam, far outboard from the mount point (Figure 13). The bottom plot is from a propeller driven run during the secondary test campaign where two sensors on the front of the beam were used. The outboard sensor was the same one from the primary test campaign and the inboard sensor an addition. The as-captured data are difficult to interpret which speaks to the limitations of how fast useful data can be read out and acted on. The data were captured at a measurement frequency of $\sim$ 200 Hz. In addition to artifacts from capturing data at high speed (low integration time) for the propeller driven runs, there was significant noise generated by the electronics and picked up by the data capture system. This noise persisted even after the CNT roving sensor wiring was changed from ribbon cables to twisted wire pairs. Capacitors

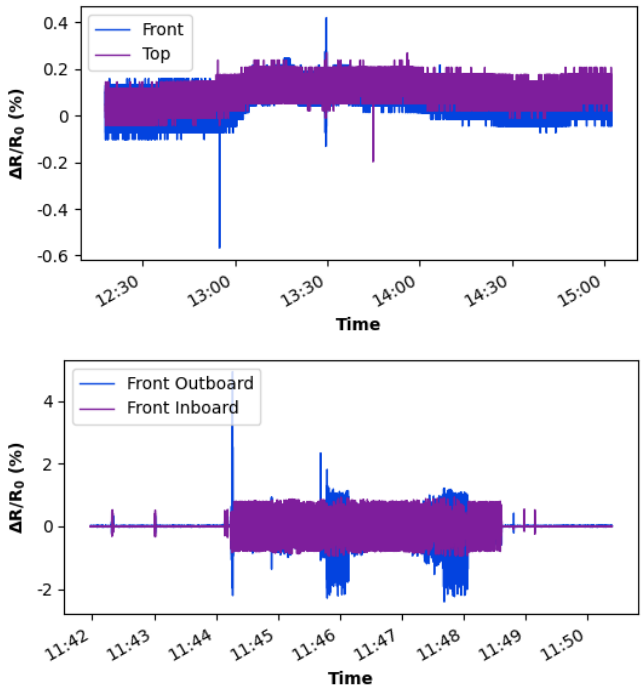

Figure 34. The as-measured responses of the CNT roving gauges show significant noise levels.

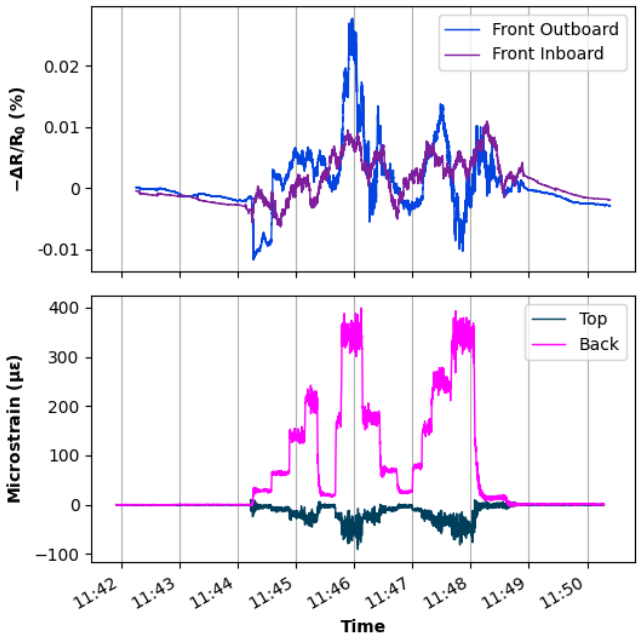

Figure 35. Plotting the averaged load step responses of the CNT roving gauges (top) and reference metal foil gauges (bottom) together show some correlation between the two sensor types.

placed in parallel with the sensors also did not immediately address the noise problem. The longer length of these specific CNT sensor devices made them perfect antennae for the noise and was a clear downside for the application.

The averaged response of the CNT roving sensors to step changes in the load are shown in Figure 35. The data were processed using a 3000 point Moving Average filter. Metal foil strain gauge data are plotted as a reference for the load condition. The steps in the CNT sensor data seem to correlate with metal foil gauge data when viewed together, but analyzing CNT roving sensor data independently would yield a significant amount of transients. The outboard sensor showed a stronger response than the sensor mounted inboard in the region of the notch.

The CNT roving gauges seem to be more sensitive to load spikes, as shown in Figure 36, than load stepping. Here, responses in the CNT roving sensor data are more easily correlated with corresponding responses in reference data from the metal foil gauges. Again, the outboard sensor shows a stronger response than the sensor mounted in-board. There is a notable asymmetry in the CNT roving sensor device response that may indicate a difference in their ability to measure compressive versus tensile strains. While the metal foil gauge data swings between -200 microstrain and $+200$ microstrain, the CNT roving sensor data $-\Delta R/R_0$ ranges from -0.04% up to only $\sim 0.008\%$.

The filtered response of the CNT roving gauges during the cam driven run of the primary test campaign are shown in Figure 37. The filtered data were obtained from the raw data plotted in Figure 34 (top). The individual cam loading cy-

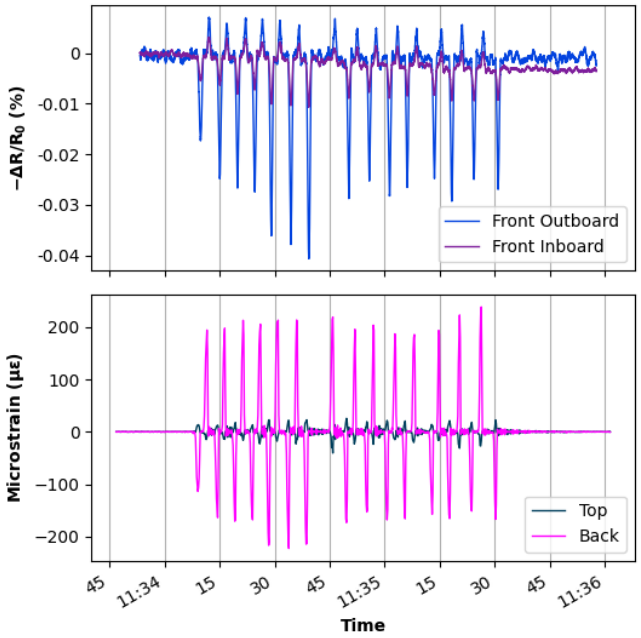

Figure 36. Plotting the averaged load spike responses of the CNT roving gauges (top) and reference metal foil gauges (bottom) together show good correlation between the two sensor types.

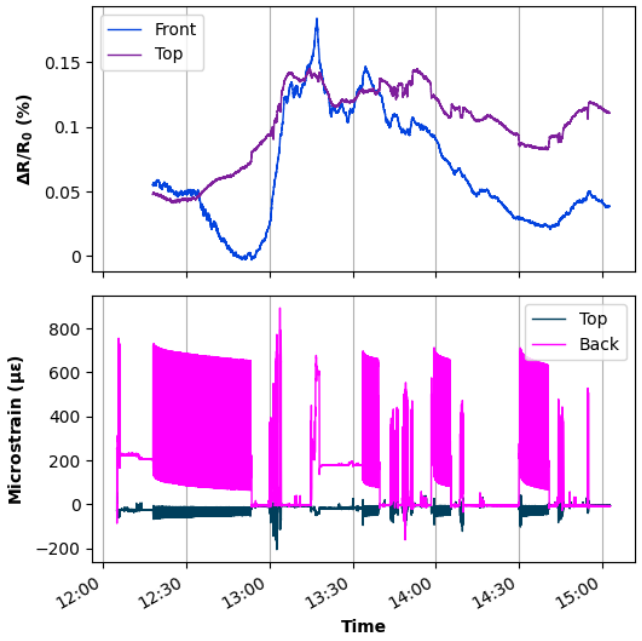

Figure 37. The filtered CNT roving gauge responses (top) compared with the reference metal foil gauges (bottom)during cam-driven fatigue cycling appears to show long-term drifts in the magnitude of $\Delta R/R_0$ in both orthogonal gauges.

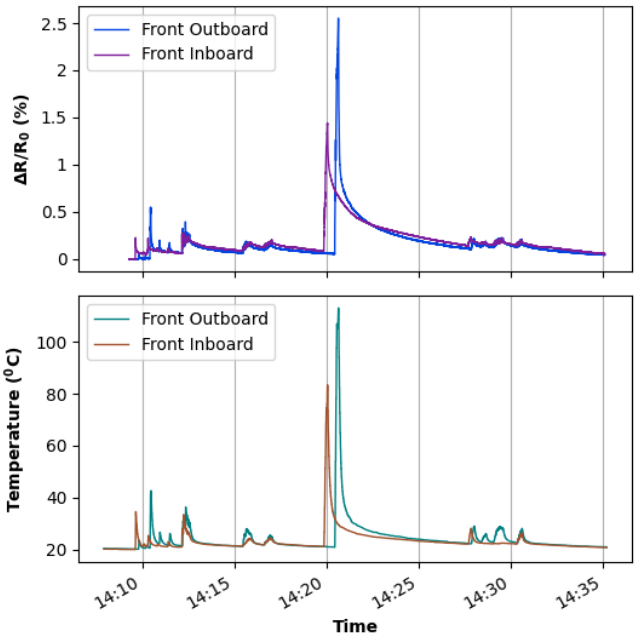

Figure 38. There is strong correlation between the temperature responses of the CNT roving gauges (top) and reference thermocouples (bottom).

cles cannot be resolved or readily matched with those from the metal foil gauges. Instead, there appear to be long-term drifts in the magnitude of $\Delta R/R_0$ that are seen in the data from both orthogonal gauges. The exact cause of this response is not clear, but temperature changes over the nearly three hours of the test may be a contributing factor. The location of the testbed and facility windows meant that for parts of the afternoon, the sun was shining on the test beam and directly onto the sensors as well. As will be shown below, an increase in the temperature of the sensors would lead to an increase in the magnitude of $\Delta R/R_0$.

As a final test of the CNT roving sensor devices, their temperature response was measured. The responses of the CNT roving gauges are shown in Figure 38. The resistances of the roving sensor devices closely track the reference thermocouple temperatures and the response is much clearer than the strain response.

Auxiliary Sensors Response

Additional sensors on the testbed and test beam provided data that proved important in monitoring and controlling the experiments. A thermal camera, thermocouples on the motor housing, and a thermistor near the motor coils provided thermal data to help warn of potential thermal runaway and meltdown. The motor thermal data heavily influenced the load steps of the tests. This mirrors operational situations in which engine/power train (including battery for electrified vehicles) anomalies are the more likely to be the determinative factors

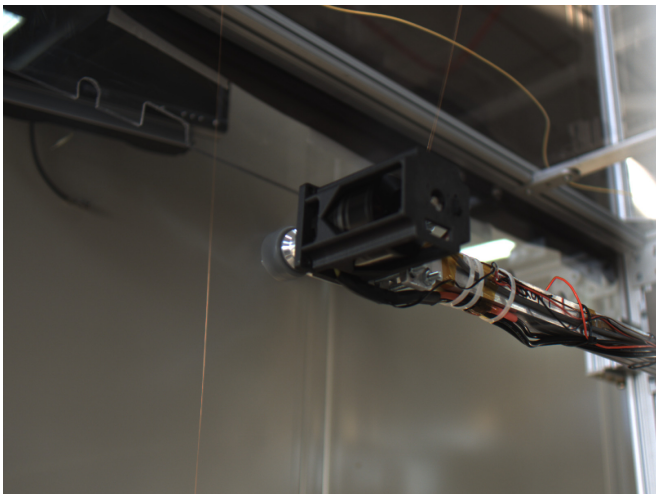

Figure 39. Video cameras continue to be a valuable auxiliary data system in a variety of test platforms. The image shows a frame captured during propulsor loading of the beam in the testbed.

for flight safety and therefore a higher priority for monitoring. Safety parameters such as high temperature limits are readily addressable using auxiliary sensors, as was the case in this experiment. Close optical imagery obtained from a camera mounted on the testbed is shown in Figure 39. A snapshot of the IR imagery available throughout the testing is shown in Figure 40.

Figure 40. IR cameras also continue to be a valuable auxiliary data system in a variety of test platforms. The image shows an IR frame captured during propulsor loading. In a future redesign of the motor housing, alterations to allow for improved air-flow within the observed hot spots would be implemented.

OBSERVATIONS AND DISCUSSION

Sensor Integration Testbed

Having a dedicated testbed proved to be a useful focal point for bringing together different sensor technologies to a common test article in order to measure related quantities simultaneously in the identical environment. Even from the initial runs, challenges that would be expected in flight, such as how specific loading conditions influence damage propagation, were encountered and needed to be addressed. Beam loads introduced solely by the propulsor were found to be inadequate for encouraging crack propagation, requiring the implementation of alternative loading methods. The flexibility of the dedicated testbed allowed for rapid set up of the cam-based loading in place of propulsor loading. Alternating between cam-based fatigue cycling and propulsor loading was easily accomplished without removing sensors. Some aspects of conditions in the testbed, such as the acoustic background environment, may be quite different from what would be encountered in flight, thus complicating the data interpretation. Such deviations will need to be better understood and addressed moving forward. Changes in equipment such as the motor mounting fixtures, cabling, and the motor controllers may also improve the fidelity of the testing relative to flight conditions.

Metal Foil Strain Gauges

The metal foil strain gauges were highly effective in measuring strains resulting from the variety of applied loads. Interpretation of single-point strain information to determine the presence or extent of damage can be challenging. The quantity and distribution of metal foil strain gauges and associated wiring are the potential limitations to their wider use in SHM. For known critical areas where strain monitoring with high confidence is needed, metal foil strain gauges remain a reliable solution (Ref. 8). Additionally, they serve as a high fidelity reference sensor for evaluation of new technologies.

Eddy Current Sensors

The custom wound pancake coil effectively tracked the initiation and growth of a fatigue crack on the representative flight component. The sensor methodology requires the placement of eddy current sensors at critical locations where fatigue damage is most likely to initiate or has already been observed. For effective use, the technique would need to be coupled with other, large area structural health monitoring sensors to effectively manage vehicle-wide risk due to crack initiation and/or growth during flight.

Fiber Optic Sensors

The fiber optic sensors were able to measure strain changes in the test beam from the baseline (before notching), through cutting, and throughout the subsequent fatigue cycling. The changes were manifested as significant relative changes in the sensor strain profiles. The interpretation of absolute strain measurement is much more difficult as there are several contributing factors to absolute strain variance.

Guided Wave Sensors

There were AE emissions for which the source has not yet been identified and these detract from the identification of events from the later runs that had crack propagation. Therefore, the baseline is not distinct enough to compare with the post-notch AE to definitively suggest which post-notch AE is crack propagation. These point to a limitation of the testbed platform, as currently implemented, that would need to be identified and resolved.

At the different stages of the testing there were obvious and significant changes in the UT pulse propagation, seen in the wavelet transforms of single pulse event waveforms. The results show that the UT sensor approach warrants additional investigation and may be a promising approach to identify damage growth. The small size and remote monitoring capability demonstrated by the spotWave system with two NDE modalities and the ability to place transducers at distances apart on a structure support continued investigation for flight operations, even if limited to ground-based static implementation.

Carbon Nanotube Roving Sensors

Fabricating sensor devices from the roving made them easier to handle and apply than the more delicate as-received CNT roving. This made deployment relatively straight forward using more traditional sensor bonding procedures and tools.

CNT roving sensors showed step response data that trended with the metal foil strain gauge data, but was not nearly as

clean and distinctive. There may be several contributors to this result. The high data capture rate and the electrical noise infiltrating the sensors were an issue. Artifacts from the data processing (moving average filter) are also a concern. Butterworth low-pass filters were tested on the data but a set of filter parameters that performed better than the moving average algorithm had not been reached. Considering the sensor device fabrication methodology, the physical size and geometry of these sensors could have made them more vulnerable to electrical noise. Note that the metal foil strain gauges, which used ribbon cables, did not pick up as much noise as the CNT roving sensors. A compact carbon resistor with the same resistance as the CNT roving sensors, which was placed in the same location as the CNT roving sensors during secondary testing, also did not experience the noise present in the CNT roving sensors. The carbon resistor was evaluated with the same data acquisition system as the roving sensors. This result indicates that the noise pick up was most likely a result of the CNT roving sensor geometry and size. Additionally, the simple procedure used to make the sensor devices may have led to poor transfer of load between the polyimide backing and the sensing roving. The adhesion between the backing and the roving was limited to the adhesion of the as-received polyimide tape.

The CNT roving sensors showed clear, albeit asymmetrical, response to sharp load pulses. These sensors were interrogated with the propulsor electronics off, eliminating that particular source of noise. It is also possible that a pulsed response is better transmitted to the roving by the obstacle that is part of the sensor device construction (Appendix). The obstacle can act as a point mass that introduces load into the roving.

The CNT roving sensors showed distinct temperature responses well above the noise level. The temperature response would be less sensitive to any poor adhesion of the roving to its backing perhaps accounting for the cleaner response.

Auxiliary Sensors

The auxiliary sensors, in particular the propulsor motor temperature probes, proved to be valuable in providing real-time information valuable in the operation and safety of the testbed itself. The health of the motor depended on keeping the motor temperature below manufacturer's recommendations, which influenced the drive levels of the propulsor. Additionally, IR imaging helped to understand the thermal profile of the motor housing, which ultimately led to a housing redesign to allow for increased air-cooling.

Data Fusion and Decision Making

Many of the instruments used during testing had standalone, dedicated DAQs and/or data capture software. How data from these disparate systems can be fused, on what time-frames, and the final format of the output remained unanswered questions. Although the testbed apparatus was a relatively simple platform to utilize, significant effort is necessary truly integrate all the data together – something that was not achieved in the current work.

CONCLUDING REMARKS

The installation of sensors onto structures, including airframes, to obtain real-time health data throughout their operational lifetime has been something of a holy grail in SHM. The vision is that a wide array of sensors would provide sufficient data to make the structures "self-aware" and impact how they are utilized, managed and maintained. Emerging UAM systems will push airframe development toward lightweight, adaptable, high-efficiency designs with SHM sensor suites helping to enable such architectures. While sensors currently play critical roles in many structures and systems, experience has shown that achieving the global coverage and reliability required for "self-aware" structures is non-trivial and not guaranteed to be solvable with currently available sensor technology. This use of on-board sensors as the primary structural health guarantor has also not been shown to be the best system level solution in all situations. In the cases where it is pursued, there must be a concerted, multi-stage effort that addresses a wide array of sensor technologies and the associated challenges of practically deploying and using them in the particular application. These challenges include the size of the sensors, mass/power/volume requirements of associated data acquisition hardware and wiring, ambiguity of the signals, sensor reliability, redundancy, and maintenance, and the additional overall system complexity resulting from the use of the sensors. Cost (both upfront and lifetime) is also an important factor, particularly in the UAM application. Adequately addressing these and other questions requires repeated tests over long campaigns with the full range of sensors that would be used in practice. A dedicated testbed that allows the investigation of the use of multiple sensor types in a relevant configuration is one such tool that would complement benchtop, crash/drop, wind tunnel and in-flight testing.

Author contact: Godfrey Sauti, Russell Wincheski, Christopher Stelter, Michael Horne, Jason Moore, Emilie Siochi.

APPENDIX

Fabrication of Carbon Nanotube Roving Sensor Devices

To fabricate the CNT roving sensors, the aerogel-spun CNT roving was purchased from Nanocomp Technologies (Hunstman Corporation) and used as-received. The roving had a linear density of 11.42 tex (g/km), tenacity of 0.45 N/tex of was and electrical resistivity of 4.42×10^{-4} Ωcm (linear resistance ~ 4 Ωcm^{-1}). Kapton tape was used as the backing for the sensors. The components for making the sensors are shown in Figure 41.

To construct a sensor device, the tape was laid adhesive side up on a flat surface. The roving was then laid onto the tape and into the adhesive with enough material at the ends for the connection tails. Steps for the fabrication of the sensors are shown

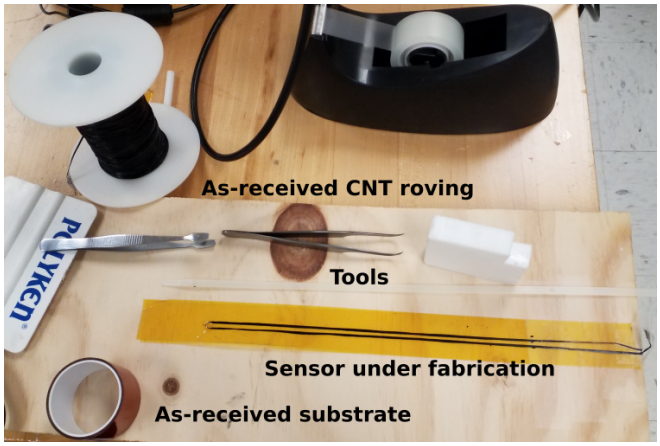

Figure 41. The primary components fabricating CNT roving sensors are the CNT roving and Kapton tape. The components are manipulated primarily with Teflon tools.

in Figure 42. A small plastic obstacle was used to tension the roving. The roving was worked into the adhesive using polytetrafluoroethylene (PTFE, Teflon) tools. After the roving was well worked into the adhesive along the entire length of the sensor, another piece of tape was then placed, adhesive side down, onto the roving. This assembly was then pressed to remove air pockets and ensure good adhesion with the roving. The tails were split aside and excess tape was trimmed. Crimping with ferrules was used to connect the CNT roving to connection leads. Additional extensions were then soldered to the leads as needed.

A completed sensor device is shown in Figure 43. Benchtop tests of sensors fabricated using this process yielded promising results for measuring strain, as shown in Figure 4, leading to their inclusion in the drop test of Figure 6 and testbed runs of this work.

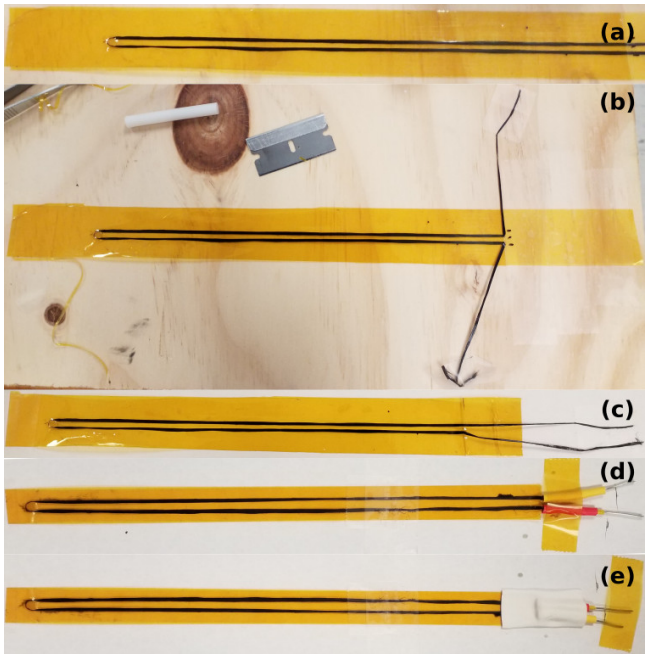

Figure 42. The steps for fabricating the sensor devices are as follows: a) CNT roving is tensioned against a small plastic object and set into the adhesive of Kapton tape, b) a second piece of Kapton tape is used to encapsulate the roving with the free ends split to the sides, c) excess tape is trimmed, d) free ends are crimped to ferrules for the electrical connections, and e) soldered wire connections are used to connect the CNT roving sensor to measurement instrumentation (not pictured).

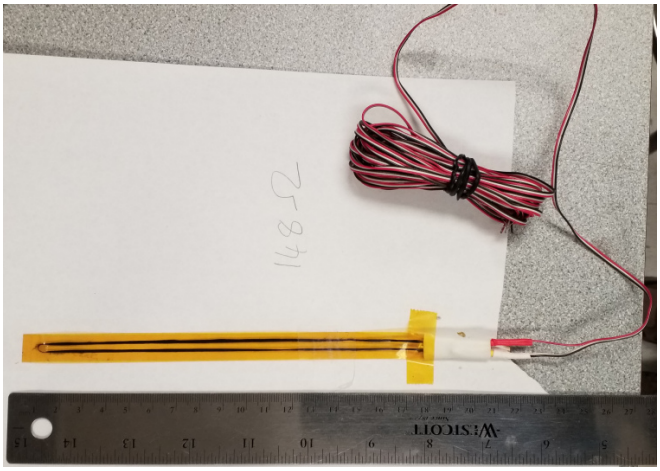

Figure 43. A completed CNT roving sensor device is approximately 17.15 cm (6.75 in.) long with a 2-wire electrical connection.

ACKNOWLEDGMENTS

The authors would like to acknowledge contributions from Hoa Luong, Lloyd Jones and Wilfredo Flores of the Materials & Structures Experiments Branch at NASA Langley Research Center in the testbed construction. Testbed computation and network resources were provided by the NASA Langley SmartLab project. Support for the current work was provided by the NASA Revolutionary Vertical Lift Technology (RVLT) program.

REFERENCES

1. Silva, C., Johnson, W. R., Solis, E., Patterson, M. D., and Antcliff, K. R., *VTOL Urban Air Mobility Concept Vehicles for Technology Development*. DOI: 10.2514/6.2018-3847.

2. Johnson, W., Silva, C., and Solis, E., "Concept Vehicles for VTOL Air Taxi Operations," , Jan 2018.

3. Johnson, W., Silva, C., and Solis, E., "Observations from Exploration of VTOL Urban Air Mobility Designs," , October 2018.

4. Reiche, C., Goyal, R., Cohen, A., and Serra, J., "Urban Air Mobility (UAM) Market Study," Technical Report

HQ-E-DAA-TN65181, Nov 2018.

5. Straubinger, A., Rothfeld, R., Shamiyeh, M., Büchter, K.-D., Kaiser, J., and Plötner, K. O., "An overview of current research and developments in urban air mobility – Setting the scene for UAM introduction," *Journal of Air Transport Management*, Vol. 87, 2020, pp. 101852. DOI: https://doi.org/10.1016/j.jairtraman.2020.101852.

6. Bristow, J. W., and Irving, P., "Safety factors in civil aircraft design requirements," *Engineering Failure Analysis*, Vol. 14, (3), UK Technical Advisory Group for Structural Integrity (TAGSI)Design margins and safety factors relating to structural integrity, 2007, pp. 459–470. DOI: https://doi.org/10.1016/j.engfailanal.2005.08.008.

7. Anon, "Maintenance Review Boards, Maintenance Type Boards and OEM/TCH Recommended Maintenance Procedures," , 2012.

8. Timothy, F., Devinder, M., and Iain, H., "F-35 Joint Strike Fighter Structural Prognosis and Health Management an Overview," ICAF 2009, Bridging the Gap between Theory and Operational Practice, edited by M. J. Bos, 2009.

9. Sun, S., Sijbers, L., Wang, X., and de Visser, C., "High-Speed Flight of Quadrotor Despite Loss of Single Rotor," *IEEE Robotics and Automation Letters*, Vol. 3, (4), 2018, pp. 3201–3207. DOI: 10.1109/LRA.2018.2851028.

10. Kessler, S. S., and Spearing, S. M., "Structural Health Monitoring of Composite Materials Using Piezoelectric Sensors," , 2016, https://www.metisdesign.com/docs/papers/materials_evaluation.pdf.

11. Hossein Montazerian, A. S. M., Armin Rashidi, and Hoorfar, M., "Integrated Sensors in Advanced Composites: A Critical Review," *Critical Reviews in Solid State and Materials Sciences*, Vol. 45, (3), 2020, pp. 187–238. DOI: 10.1080/10408436.2019.1588705.

12. Arena, M., and Viscardi, M., "Strain State Detection in Composite Structures: Review and New Challenges," *Journal of Composites Science*, Vol. 4, (2), 2020.

13. Belcastro, C. M., "Integrated Resilient Aircraft Control (IRAC): Research Overview," , October 2006, https://acgsc.org/Meetings/Meeting_98/General%20Session/4.1.4.3.ppt.

14. Hanson, C. E., "Capability Description for NASA's F/A-18 TN 853 as a Testbed for the Integrated Resilient Aircraft Control Project," Technical Report DFRC-IRAC-CAP-002, January 2009.

15. Bosworth, J. T., "Integrated Resilient Aircraft Control Project Full Scale Flight Validation," , August 2009.

16. Gregory, I. M., Leonard, C., and Scotti, S. J., *Self-Aware Vehicles: Mission and Performance Adaptation to System Health Degradation*. DOI: 10.2514/6.2016-3165.

17. Iscold, P., and Fladung, W., "Aeroelastic Test of the Nixus FBW Sailplane," Sensors and Instrumentation, Aircraft/Aerospace, Energy Harvesting & Dynamic Environments Testing, Volume 7, edited by C. Walber, M. Stefanski, and S. Seidlitz, 2022.

18. Woodard, S. E., "Functional Electrical Sensors as Single Component Electrically Open Circuits Having No Electrical Connections," *IEEE Transactions on Instrumentation and Measurement*, Vol. 59, (12), 2010, pp. 3206–3213. DOI: 10.1109/TIM.2010.2047546.

19. DiGiampaolo, E., DiCarlofelice, A., and Gregori, A., "An RFID-Enabled Wireless Strain Gauge Sensor for Static and Dynamic Structural Monitoring," *IEEE Sensors Journal*, Vol. 17, (2), 2017, pp. 286–294. DOI: 10.1109/JSEN.2016.2631259.

20. Gao, S., Dai, X., Hang, Y., Guo, Y., and Ji, Q., "Airborne Wireless Sensor Networks for Airplane Monitoring System," *Wireless Communications and Mobile Computing*, Vol. 2018, May 2018, pp. 6025825. DOI: 10.1155/2018/6025825.

21. Kopsaftopoulos, F., Nardari, R., Li, Y.-H., and Chang, F.-K., "A stochastic global identification framework for aerospace structures operating under varying flight states," *Mechanical Systems and Signal Processing*, Vol. 98, 2018, pp. 425–447. DOI: https://doi.org/10.1016/j.ymssp.2017.05.001.

22. Yuan, F.-G., Zargar, S. A., Chen, Q., and Wang, S., "Machine learning for structural health monitoring: challenges and opportunities," Sensors and Smart Structures Technologies for Civil, Mechanical, and Aerospace Systems 2020, edited by H. Huang, H. Sohn, and D. Zonta, Vol. 11379, Society of Photo-Optical Instrumentation Engineers (SPIE) Conference Series, apr 2020. DOI: 10.1117/12.2561610.

23. Amer, A. W., Roy, S., and Kopsaftopoulos, F., *Probabilistic SHM under varying loads via the integration of Gaussian Process Regression and physics-based guided-wave propagation models*. DOI: 10.2514/6.2021-0434.

24. Matos, M. A., Pinho, S. T., and Tagarielli, V. L., "Application of machine learning to predict the multiaxial strain-sensing response of CNT-polymer composites," *Carbon*, Vol. 146, 2019, pp. 265–275. DOI: https://doi.org/10.1016/j.carbon.2019.02.001.

25. Anon, "AE3145 Resistance Strain Gage Circuits," , 2000, https://studylib.net/doc/18216602/resistance-strain-gage-circuits.

26. McMaster, R. C., and Udpa, S., Nondestructive Testing Handbook, Second Edition, Electromagnetic Testing, edited by P. Mcintire, 1986.

27. Libby, H. L., *Introduction to Electromagnetic Nondestructive Test Methods*, Wiley-Interscience, New York, 1971.

28. Jackson, J. D., *Classical Electrodynamics*, John Wiley and Sons, New York, 1962, pp. 209–213.

29. Prosser, W. H., Wincheski, R. A., Saulsberry, R. L., Nichols, C. T., Lucero, R. E., Milana, A. M., Dawicke, D. S., and Spencer, F. W., "Composite Overwrapped Pressure Vessel (COPV) Liner Inspection Capability Development Assessment," Technical Report NASA TM20205002461, NASA Langley Research Center, Hampton, VA, May 2020.

30. Chen, T., He, Y., and Du, J., "A High-Sensitivity Flexible Eddy Current Array Sensor for Crack Monitoring of Welded Structures under Varying Environment," *Sensors*, Vol. 18, (6), 2018. DOI: 10.3390/s18061780.

31. Goldfine, N., Zilberstein, V., Schlicker, D., and Grundy, D., *Eddy-Current in situ Sensors for SHM*, John Wiley & Sons, Ltd, 2009. DOI: https://doi.org/10.1002/9780470061626.shm080.

32. Mandache, C., Lapointe, J., and Genest, M., "Mounted Eddy Current Sensors for Monitoring Structural Degradation," , 2016, https://www.ndt.net/events/NDTCanada2016/app/content/Slides/30_Mandache.pdf.

33. Eddyfi NDT, Inc, *Eddyfi Reddy User's Guide*, 2017.

34. Kersey, A. D., Davis, M. A., Patrick, H. J., LeBlanc, M., Koo, K., Askins, C., Putnam, M., and Friebele, E. J., "Fiber grating sensors," *Journal of lightwave technology*, Vol. 15, (8), 1997, pp. 1442–1463.

35. Childers, B. A., Froggatt, M. E., Allison, S. G., Moore Sr, T. C., Hare, D. A., Batten, C. F., and Jegley, D. C., "Use of 3000 Bragg grating strain sensors distributed on four 8-m optical fibers during static load tests of a composite structure," Smart structures and materials 2001: Industrial and commercial applications of smart structures technologies, Vol. 4332, 2001.

36. Beemer, R., Cassidy, M., and Gaudin, C., "Investigation of an OFDR fibre Bragg system for use in geotechnical scale modelling," Physical Modelling in Geotechnics, Volume 1: Proceedings of the 9th International Conference on Physical Modelling in Geotechnics (ICPMG 2018), July 17-20, 2018, London, United Kingdom, 2018.

37. Soller, B. J., Gifford, D. K., Wolfe, M. S., and Froggatt, M. E., "High resolution optical frequency domain reflectometry for characterization of components and assemblies," *Optics Express*, Vol. 13, (2), 2005, pp. 666–674.

38. Moore, J. P., "Basic Theory and Operating Principles of Optical Frequency Domain Reflectometry Measurement Systems as Applied to Fiber Bragg Grating Sensors," Technical Report NASA-TP-20230005269, NASA Langley Research Center, Hampton, VA, May 2023.

39. Othonos, A., and Kalli, K., *Fiber Bragg Gratings: Fundamentals and Applications in Telecommunications and Sensing*, Artech House, 1999.

40. Rose, J. L., *Ultrasonic Guided Waves in Solid Media*, Cambridge University Press, New York, NY 10013-2473. USA, 2014.

41. G. L. Workman and P. O. Moore, editors, *Nondestructive Testing Handbook, Vol. 10: Overview*, American Society for Nondestructive Testing, third edition, 2012.

42. Leckey, C., Frankforter, E., Horne, M., and Schneck, W., "Modeling of guided waves for aerospace applications," SPIE Proceedings Vol. 11593: Health Monitoring of Structural and Biological Systems XV, edited by P. Fromme and Z. Su, 2021. DOI: 10.1117/12.2584369.

43. Koziol, K., Vilatela, J., Moisala, A., Motta, M., Cunniff, P., Sennett, M., and Windle, A., "High-Performance Carbon Nanotube Fiber," *Science*, Vol. 318, (5858), 2007, pp. 1892–1895. DOI: 10.1126/science.1147635.

44. Kim, J.-W., Sauti, G., Siochi, E. J., Smith, J. G., Wincheski, R. A., Cano, R. J., Connell, J. W., and Wise, K. E., "Toward High Performance Thermoset/Carbon Nanotube Sheet Nanocomposites via Resistive Heating Assisted Infiltration and Cure," *ACS Applied Materials & Interfaces*, Vol. 6, (21), PMID: 25325388, 2014, pp. 18832–18843. DOI: 10.1021/am5046718.

45. Hossain, M. M., Lubna, M. M., and Bradford, P. D., "Multifunctional and Washable Carbon Nanotube-Wrapped Textile Yarns for Wearable E-Textiles," *ACS Applied Materials & Interfaces*, Vol. 15, (2), PMID: 36622361, 2023, pp. 3365–3376. DOI: 10.1021/acsami.2c19826.

46. Yao, X., Hawkins, S. C., and Falzon, B. G., "An advanced anti-icing/de-icing system utilizing highly aligned carbon nanotube webs," *Carbon*, Vol. 136, 2018, pp. 130–138. DOI: https://doi.org/10.1016/j.carbon.2018.04.039.

47. Kessler, S. S., Thomas, G., Borgen, M. G., and Dunn, C. T., "Carbon Nanotube Appliques for Fatigue Crack Diagnostics," *Structural Health Monitoring-an International Journal*, 2015.

48. Kang, I., Schulz, M. J., Kim, J. H., Shanov, V., and Shi, D., "A carbon nanotube strain sensor for structural health monitoring," *Smart Materials and Structures*, Vol. 15, (3), apr 2006, pp. 737. DOI: 10.1088/0964-1726/15/3/009.

49. Obitayo, W., and Liu, T., "A Review: Carbon Nanotube-Based Piezoresistive Strain Sensors," *Journal of Sensors*, Vol. 2012, Apr 2012, pp. 652438. DOI: 10.1155/2012/652438.

50. FBGS, 2023, https://fbgs.com/components/all-grating-fibers-agf/.

51. Keithley, *Model DMM7510 7½ Digit Graphical Sampling Multimeter Reference Manual*, May 2015.